Publication Year	2022
Acceptance in OA	2022-03-28T09:39:53Z
Title	Macro and micro structures of pebble-made cometary nuclei reconciled by seasonal evolution
Authors	CIARNIELLO, Mauro, FULLE, Marco, RAPONI, Andrea, FILACCHIONE, GIANRICO, CAPACCIONI, FABRIZIO, Rotundi, Alessandra, RINALDI, GIOVANNA, FORMISANO, Michelangelo, Magni, Gianfranco, TOSI, Federico, DE SANCTIS, MARIA CRISTINA, CAPRIA, MARIA TERESA, LONGOBARDO, ANDREA, Beck, Pierre, FORNASIER, SONIA, Kappel, David, MENNELLA, Vito, Mottola, Stefano, ROUSSEAU, BATISTE PAUL RAYMOND, Arnold, Gabriele
Publisher's version (DOI)	10.1038/s41550-022-01625-y
Handle	http://hdl.handle.net/20.500.12386/31932
Journal	NATURE ASTRONOMY
Volume	6

Seasons of comets reconcile the macro and micro structures of nuclei

Mauro Ciarniello[1,*], Marco Fulle[2], Andrea Raponi[1], Gianrico Filacchione[1], Fabrizio Capaccioni[1], Alessandra Rotundi[3,1], Giovanna Rinaldi[1], Michelangelo Formisano[1], Gianfranco Magni[1], Federico Tosi[1], Maria Cristina De Sanctis[1], Maria Teresa Capria[1], Andrea Longobardo[1], Pierre Beck[4,5], Sonia Fornasier[5,6], David Kappel[7,8], Vito Mennella[9], Stefano Mottola[7], Batiste Rousseau[1], and Gabriele Arnold[7]

[1]IAPS-INAF, Istituto di Astrofisica e Planetologia Spaziali, Rome, Italy.
[2]INAF - Osservatorio Astronomico, Trieste, Italy.
[3]Universitá degli Studi di Napoli Parthenope, Dip. di Scienze e Tecnologie, Naples, Italy.
[4]Université Grenoble Alpes, CNRS, IPAG, Grenoble, France.
[5]Institut Universitaire de France (IUF), Paris, France.
[6]LESIA, Observatoire de Paris, Université PSL, CNRS, Université de Paris, Sorbonne Université, Meudon, France.
[7]Institute for Planetary Research, German Aerospace Center (DLR), Berlin, Germany.
[8]Institute of Physics and Astronomy, University of Potsdam, Potsdam, Germany
[9]INAF—Osservatorio Astronomico di Capodimonte, Naples, Italy.
[*]mauro.ciarniello@inaf.it

Summary

Observations of comets from space missions showed puzzling water-ice-rich spots, distributed across the nucleus surface[1–5]. These areas are up to tens of metres large, and stand out as optically brighter and spectrally bluer patches than the average low albedo cometary surface. Here, we show that the occurrence of the Blue Patches (BPs) observed by the Rosetta mission[6] at comet 67P/Churyumov-Gerasimenko opens a window into the cometary interior structure. The interior structure reveals itself through seasonal variability of the nucleus color[7–9] and is well described by recent cometary activity models[10,11]. We explain the presence of the BPs as the exposed counterpart of sub-metre-sized Water-ice-Enriched Blocks (WEBs) distributed within the nucleus interior. The emergence of BPs is connected with the nucleus surface erosion induced by CO_2-ice sublimation, which increases the BP amount when the comet is close to the Sun. WEBs, in turn, are eroded by water-ice sublimation when exposed to illumination as BPs. Our findings imply an uneven water-ice distribution in comets, with inhomogeneities at scales larger than the cm-sized pebbles composing their nuclei[12], for which we define a new model of internal structure (Fig. 1).

Seasonal colour cycle

In their orbit around the Sun cometary nuclei evolve under the effects of gaseous activity. Ices sublimation induces dust emission, i.e. erosion, followed by mass loss, mass redistribution and surface modifications. First examples of surface changes on a comet were revealed by the Deep Impact and Stardust-NEXT missions for 9/Tempel 1[14], while a full inventory of the processes shaping cometary nuclei has been provided by Rosetta escorting 67P/Churyumov-Gerasimenko (hereafter 67P) for approximately two years[15–18]. Rosetta revealed also compositional variations of the comet surface, with the occurrence of diurnal[8,19] and seasonal cycles[8,9,20] modulating the water-ice abundance. The seasonal increase of

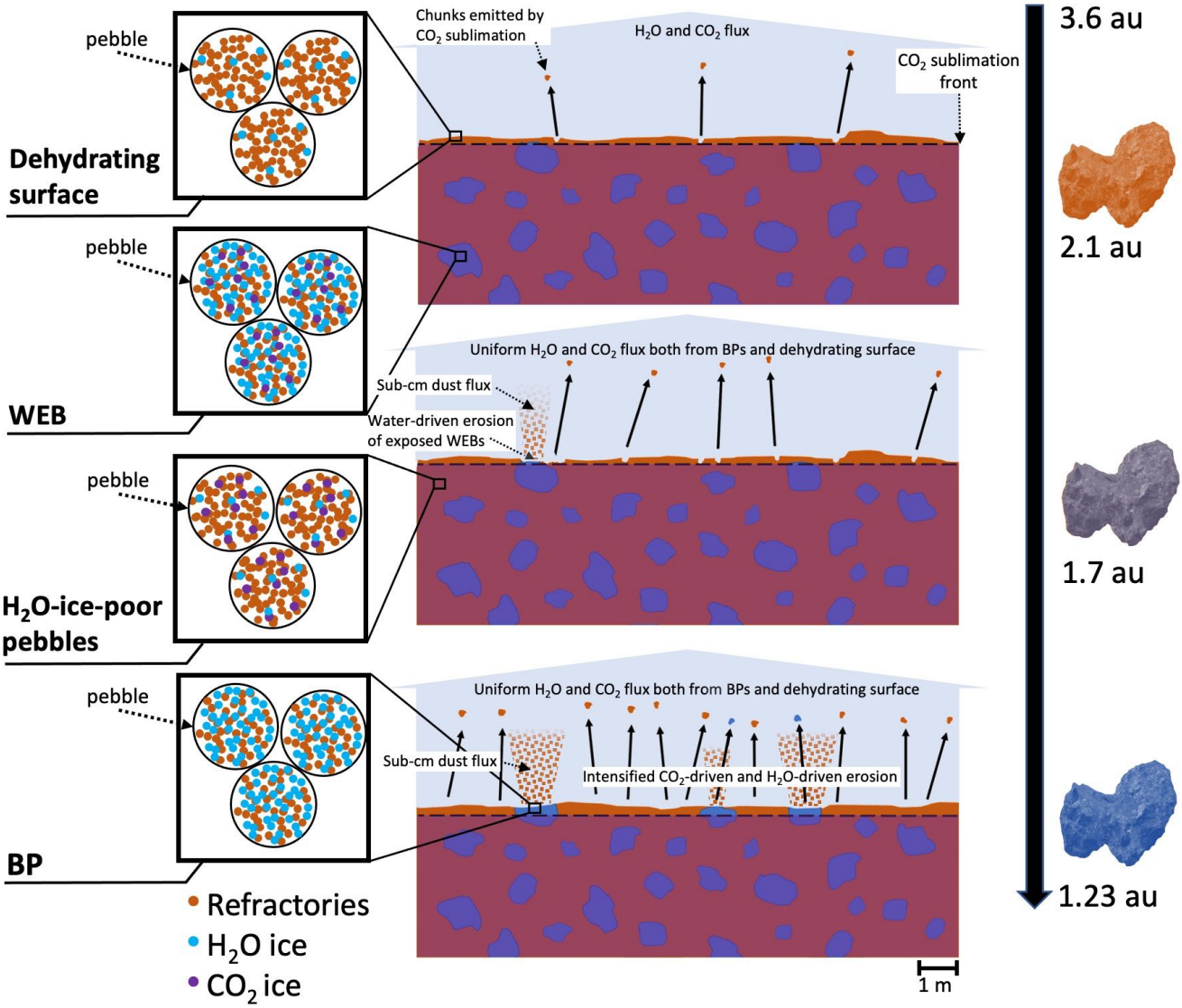

Figure 1. 67P surface blueing at perihelion is due to the progressive exposure to sunlight of subsurface Water-Ice-Enriched Blocks (WEBs). The comet nucleus is composed of two types of pebbles made of refractories and CO_2 ice plus: 1) high content of H_2O ice, forming the WEBs; 2) low content of H_2O ice (H_2O-ice-poor pebbles, compatible with the material observed during the occasional exposure of CO_2-ice by ref.[13]), composing most of the nucleus. CO_2 ice survives under the CO_2 condensation front at depths > 0.1 m (ref.[11]). Its sublimation rate increases approaching perihelion, eroding the surface by chunk ejection and exposing the sub-surface WEBs. After exposure, WEBs lose their CO_2 becoming BPs; water-ice sublimation erodes the BPs, while removing dust from their surface and preventing the formation of a dry crust[10]. The BPs survive as such until the complete sublimation of their water-ice fraction, and long enough to induce the observed surface blueing. Dehydration overcomes erosion in the H_2O-ice-poor pebbles[10], whereas the formation of a crust is prevented by the ongoing CO_2-driven erosion. BPs and dehydrating surface eject the same water flux, because both have some water ice inside and are assumed at the same temperature[10].

exposed H_2O ice on 67P approaching perihelion has been qualitatively interpreted as the effect of cometary activity enhancement[21] giving access to subsurface ice by progressive dust removal[7–9,22,23]. The recent development of nucleus thermal models, the first ones consistent with dust ejection in a nucleus made of pebbles[12], for water-driven[10] and CO_2-driven activity[11], allowed us to couple quantitatively the water-ice seasonal cycle to cometary activity.

The Mapping channel of the Visible, Infrared and Thermal Imaging Spectrometer (VIRTIS-M)[24] observed the 67P's surface throughout the whole Rosetta mission with its visible (VIS) channel (0.2-1 μm). Previous studies[3,7,22], supported by the availability of infrared observations during part of the inbound orbit (August 2014 - April 2015), correlated the VIS colour to superficial water-ice abundance: lower spectral slopes (bluer) indicating larger amounts of water ice. Here, we exploit the whole VIRTIS-M/VIS channel dataset of nucleus observations (August 2014 - September 2016) to systematically characterise the surface water-ice seasonal variations. We produced maps of spectral slope in the 0.55-0.8 μm interval to monitor the spatial and temporal variability of 67P surface colour along the orbit, as reported in Fig. 2 (see Supplementary Information for spectral-slope computation, data calibration refinement and maps production). The August 2014 spectral-slope map reflects the dichotomy characterising the 67P surface colour, with the Hapi morphological region, at northern latitudes, being distinctively bluer than the rest of the nucleus, as a result of a larger content of water ice[7,25,26]. Hapi is located in the "neck" that connects the two main lobes composing the 67P nucleus[27]. Due to the inclination of the comet's rotation axis (obliquity of 52.4°) the summer of northern and southern regions occurs in different orbital phases: the northern hemisphere is most illuminated at large heliocentric distances, whereas the southern hemisphere is most illuminated from May 2015 to March 2016 when the comet is at less than 2.6 au (ref.[28,29]) across perihelion passage. Equatorial regions are illuminated during most of the orbit and have been systematically imaged by VIRTIS-M. These regions are characterised by a redder spectrum with respect to Hapi in August 2014, and get globally bluer approaching the Sun. The minimum spectral slope is reached around perihelion, while the original colours are gradually restored outbound from perihelion. Such temporal evolution is in agreement with the Optical, Spectroscopic, and Infrared Remote Imaging System (OSIRIS)[30] findings[8] that also show a global colour variation of the nucleus.

We selected five regions of interest (ROIs, Fig. 2) that are illuminated and observed throughout most of the mission, to monitor in more detail the spectral-slope behaviour from August 2014 to September 2016, with a temporal sampling of 30 days (Fig. 3). All the ROIs display a similar evolution of the surface colour, with maximum blueing reached around perihelion (1.23 au, August 2015), and a spectral-slope reduction of the order of $\approx 15-25\%$ compared to August 2014 (≈3.5 au, inbound). In September 2016 (≈3.8 au, outbound), the spectral slope returned to approximately the same values measured on August 2014. The common spectral evolution observed on the selected ROIs, in addition to the fairly uniform colour variability resulting from the spectral-slope mapping, indicates that the progressive enrichment of water ice at smaller heliocentric distances is a global process occurring on the whole comet surface, with the exception of the Hapi region, which is not illuminated at perihelion.

Colour temporal evolution and cometary activity

Although the colour evolution implies a global water-ice enrichment approaching perihelion, water ice is characterised by a patchy distribution across the surface of comet 67P. This is indicated by the occurrence of localised ice-rich features up to few tens of metres in size, observed by the Rosetta imaging experiments[2–4]. These areas display a higher albedo and a distinctively smaller spectral slope at visible wavelengths with respect to the surrounding terrains[18], thus appearing as BPs.

The presence of discrete ice-rich sources is also inferred from the dust ejection rates at perihelion[31]

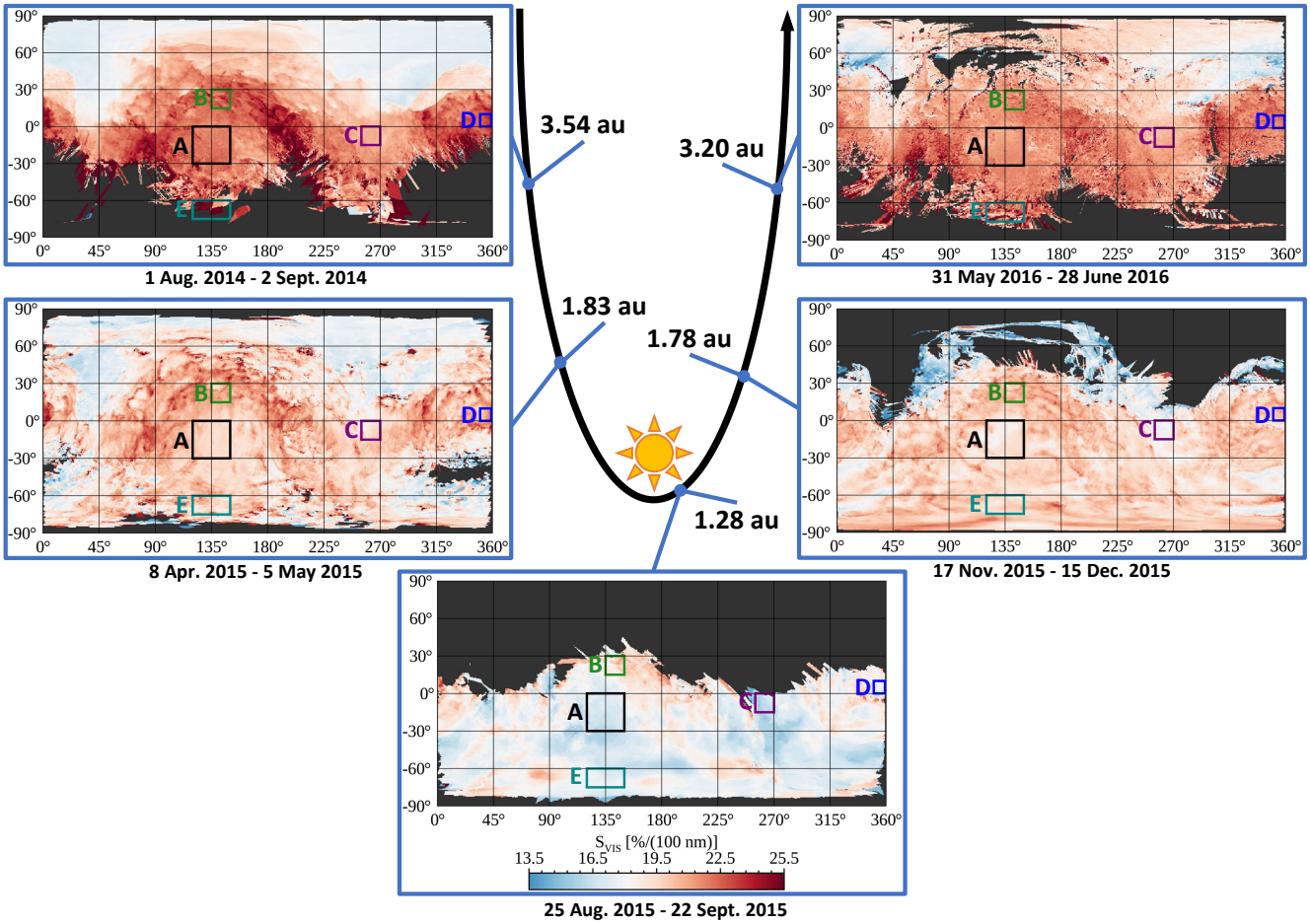

Figure 2. VIS spectral-slope (S_{VIS}) maps of comet 67P/Churyumov-Gerasimenko's surface at different orbital phases. The panel shows the evolution of the comet's colour along the inbound orbit, close to perihelion, and during the outbound orbit (see Table S1 in Supplementary Material for additional information). Surface colour gets progressively bluer inbound, when the comet approaches the Sun (perihelion at 1.23 au on 13 August 2015), followed by a reddening during the outbound phase. Solid coloured rectangles border five regions of interest (ROIs, Table S2) for which the temporal evolution of the spectral slope is monitored in Fig. 3.

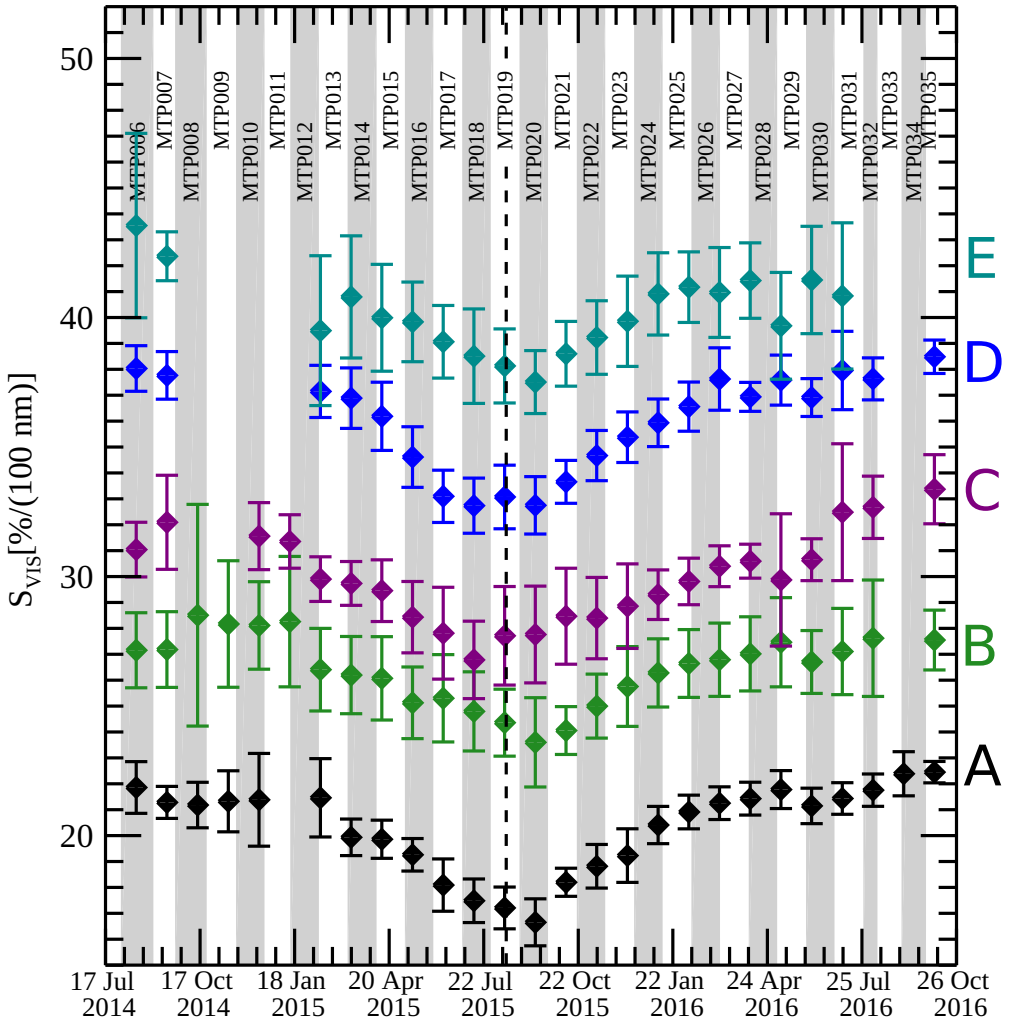

Figure 3. Spectral-slope (S_{VIS}) temporal evolution from August 2014 to September 2016, for different areas on 67P's surface. Each curve corresponds to one of the five different ROIs shown on Fig. 2, indicated by letters. From bottom to top, the curves are offset by +5 %/(100 nm). Each point and the corresponding error bars represent the spectral-slope average value and standard deviation, respectively, computed over a 30 days bin from all the observations falling in the corresponding ROI, after sigma-clipping. The Medium Term Planning (MTP) phases of the Rosetta mission and the perihelion date (dashed line) are indicated.

measured by GIADA (Grain Impact Analyser and Dust Accumulator)[32]. Cometary dust ejection is principally driven by H_2O and CO_2 ices sublimation. Water-driven erosion ejects sub-cm dust[10], while the dust volume distribution in 67P's coma is dominated by decimetre-sized chunks[31,33,34] which can be emitted only by CO_2-ice sublimation, occurring at greater depth with respect to water ice, given the deeper sublimation front[11,35,36]. Activity models[10] of water-ice sublimation and vapour diffusion inside the cm-sized pebbles making-up a cometary nucleus[12] are consistent with the observed sub-cm dust fluxes[31] if only up to $\approx 6\%$ (see ref.[10] and Methods) of the southern hemisphere undergoes erosion as a consequence of dust ejection induced by water-ice sublimation. According to ref.[10] the water-driven activity is regulated by the refractory-to-water-ice mass ratio δ. For values of the δ ratio lower than 5, sources in the southern hemisphere at perihelion are rich enough in water to sustain sub-cm dust ejection through water-ice sublimation. Conversely, for larger values of δ, water-driven erosion dies out and the surface material is dehydrated until ejected by CO_2 sublimation in the form of dm-sized chunks. This exposes underlying pebbles, activating their water-driven erosion or dehydration according to the corresponding δ.

Areas where the water-ice-driven erosion exposes the ice inside the pebbles are characterised by a spectral slope bluer than most of the surface, which is ice-poor and spectrally redder. According to this scenario the comet's surface can be described by a geographical mixture of water-ice-rich (water-driven eroded) and water-ice-poor (dehydrating) areas, with the former having an observational counterpart in the BPs.

From this, it follows that the observed seasonal colour evolution is produced by the temporal evolution of the nucleus surface fraction covered by BPs. High-resolution observations of BPs on 67P's surface indicate a volumetric ice fraction as high as 50% (ref.[5,37]), which proves that these areas, having a low-enough refractory-to-water-ice mass ratio, effectively sustain water-driven erosion. In Methods (Fig. 6) we show that there is a direct correlation between surface temperature (and by consequence heliocentric distance) and the maximum value of the δ ratio still compatible with water-driven erosion. Assuming all the BPs are characterised by a similar characteristic water-ice content (same δ), the condition for water-driven erosion in the southern hemisphere at perihelion (δ<5, ref.[10]) ensures their water-driven erosion also at larger heliocentric distances. Areas with $\delta >> 5$ are eroded by water-ice sublimation only at large heliocentric distances, and are progressively dehydrated approaching the Sun if not refreshed by CO_2-driven erosion.

By modelling (see Supplementary Information) the observed spectral-slope temporal evolution we estimate the corresponding variation of the 67P surface fraction covered by BPs. We perform this computation for the ROI A being the region characterised by the best observation conditions and smallest uncertainties on the spectral-slope values (Fig. 4). As ROI A is located in the centre of the Imhotep morphological region (see Table S2), we refer to it as the Imhotep ROI. We can compare our evaluation with the independent estimate of the fraction of areas undergoing water-driven erosion required to match the dust ejection rate (Q_d) measured in March 2015 by the GIADA experiment[31]. In fact, assuming Imhotep as the main source of activity in March 2015, we estimate from cometary activity modelling (see Methods) an average daytime erosion rate E_{day} of 5.6 cm/day and a gas emission rate $Q_g(T)$ of 5×10^{-6} kg/m^2/s as computed at the maximum temperature experienced in Imhotep (T =247 K, see methods and Fig. 6). With this value of Q_g the maximum liftable size of the ejected dust is 1 cm (ref.[38]). In this period, GIADA measured a dust flux of 20-40 kg/s for particle sizes <1 cm. The total dust flux if Imhotep were uniformly ejecting sub-cm dust can be computed as $Q_d = A \cdot \rho_d \cdot E_{day} \approx 2600$ kg/s, where $A \approx 5$ km^2 is the Imhotep area[39] and $\rho_d \approx 800$ kg/m^3 is the average dust density[31]. This value is 65-130 times larger than the one measured by GIADA, implying that approximately only 0.8-1.5% of Imhotep is ejecting sub-cm dust. In the same period, modelling the VIRTIS results provides a BP fraction comprised between 0.3% and 0.9% in the Imhotep ROI. Assuming these values as representative of the entire Imhotep region, the

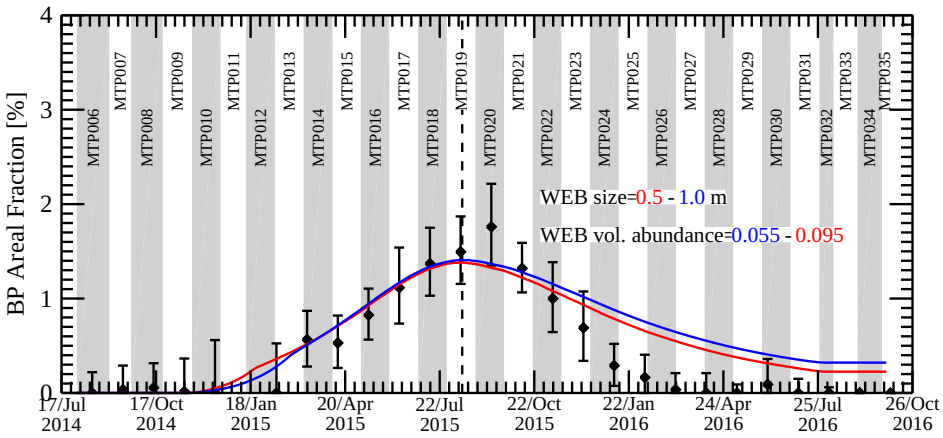

Figure 4. Temporal evolution of the BP areal fraction in the Imhotep ROI. Diamonds indicate the BP areal fraction estimated from the S_{VIS} temporal profile. The coloured lines are best-fit models (from Fig. 10b,c) of the BP temporal evolution as the effect of CO_2-driven and water-driven erosion (see Methods). After December 2015, the observed BP temporal evolution is also affected by fallout of dehydrated material ejected at perihelion (see Supplementary Material). For each model, the WEB size and the WEB volumetric abundance in the nucleus are indicated. The perihelion passage is marked by the vertical dashed line.

estimated BP fraction is compatible with the fraction of surface ejecting sub-cm dust derived from the dust ejection rate. Moreover, the observed surface blueing is compatible with a surface fraction getting covered in BPs for a maximum of 1.4-2.2 % around perihelion, decreasing at larger heliocentric distances (Fig. 4). Extrapolating the result obtained at perihelion for Imhotep to the southern hemisphere (see Supplementary Information), the derived maximum BP areal fraction is compatible with the upper limit of areal fraction characterised by water-driven activity as estimated from observed dust ejection rates[10,31] ($\approx 6\%$).

We also took into consideration an alternative scenario (see Supplementary Information), in which the observed surface colour variability is due to the seasonal variation of the thickness of a "semi-transparent" dehydrated crust on top of an active subsurface ice-rich layer (a paradigm common to most thermophysical models of comets[28,35,40]). This would affect the intensity of the subsurface ice spectral signal reaching the observer and by consequence the surface colour. However, this approach implies that the nucleus colour should depend on its surface temperature. This result is inconsistent with VIRTIS data, which indicate that Hapi and Imhotep have similar colours at different surface temperature and vice versa. Also, it is not consistent with a pebble-made nucleus, where the crust must be at least as thick as a pebble[10], thus being totally opaque to the radiation in the VIRTIS spectral range.

Modelling the BP temporal evolution

Nucleus erosion on 67P is dominated by CO_2-driven chunk emission[31,33,34]. Explaining the colour seasonal cycle of the 67P nucleus as the effect of the occurrence of BPs, implies that CO_2 erosion exposes new Water-Ice-Enriched Blocks (WEBs) present in the subsurface of the nucleus which then become BPs at the surface. The exposure of new BPs depends on the CO_2-driven erosion rate and the volumetric abundance of the WEBs in the nucleus. After exposure, BPs are eroded with a time scale primarily depending on the water-driven erosion rate and on the typical size of the WEBs (the CO_2-driven erosion of Imhotep's BPs is much slower than the water-driven one, see Methods). In order to provide the observed

blueing, the WEBs must be large enough to survive the time required to build up the observed BP areal fraction close to perihelion. Thus, the temporal evolution of a cometary nucleus colour, and in particular the observed blueing of 67P at perihelion, is due to the balance between two competing mechanisms: CO_2-driven erosion, which exposes new BPs, and water-driven erosion, occurring in the BPs, which removes them (Fig. 1). This balance, in turn, depends on the surface insolation conditions, which modulate seasonally the H_2O- and CO_2-driven erosion rates. In Methods, we report a detailed modelling of the temporal evolution of the BP areal fraction on the 67P nucleus undergoing H_2O- and CO_2-driven erosions. We apply our simulations to the Imhotep ROI case (see Fig. 4 and complete results in Fig. 10 and 11), assuming an average erosion in the region of $\lesssim 0.5$ m during one orbit[41,42]. Depending on the volumetric abundance of the WEBs in the nucleus, we find that these must be sub-metre-sized to match the observed surface colour variability up to the maximum blueing. After perihelion, the surface in the Imhotep ROI gets progressively redder while receding from the Sun: according to our simulations this is due to a progressive reduction of the WEBs exposure rate along the outbound orbit as the CO_2 activity decreases and to the cumulative back fall of dehydrated material ejected at perihelion, blanketing the comet surface and covering the BPs[40,43,44].

To further constrain the typical WEB size, we computed the expected areal fraction of BPs in the active southern hemisphere at perihelion (see Methods) as a function of volumetric abundance in the nucleus and size of the WEBs as obtained from the Imhotep ROI analysis. Assuming a total erosion from CO_2-driven chunk emission of $\approx$ 4-10 m (ref.[10,34]), we find that only WEBs with size in the $\approx 0.5-1$ m range and volumetric abundance in the nuclues from $\approx$ 9.5 % to 5.5 % are compatible with the $\approx$ 6% active areas (i.e BPs) upper limit inferred from the measured dust ejection rates[10,31]. We interpret the estimated size as referred to the dominant one in the WEB size distribution. Sub-metre WEBs are compatible with CONSERT radar observations, which indicate a mostly homogeneous 67P nucleus interior structure down to a few-metres scale[45]. Also, given the large comet-spacecraft distance around perihelion, BPs of similar size would be resolved by the OSIRIS Narrow Angle Camera (nominal spatial resolution $\approx$ 14 times better than VIRTIS') typically only before May 2015 and after mid-December 2015, when their abundance is however small (see Methods). Nonetheless, BPs up to tens of metres have been also observed on 67P's surface[3,4,22], sampling the large size tail of the WEB size distribution.

As large part of the nucleus surface displays a colour variability similar to the Imhotep ROI (Figs. 2 and 3), we infer that the mechanism described above acts on the comet surface at global scale, with the exception of most of the northern deposits (e. g. Hapi) not illuminated at perihelion, and blanketed by back fall material from the southern hemisphere during the northern winter. The low spectral slope of the Hapi deposits in August 2014, corresponding to a larger surface water ice content with respect to most of the nucleus, is indeed compatible with an origin of this material from the southern hemisphere active at perihelion[43] (see Supplementary Information).

A new nucleus model

Our results indicate that a model of the comet nucleus made of pebbles and including a uniform distribution of WEBs (Fig. 1) explains the observed surface colour temporal evolution on 67P and the observed dust ejection rates. This paradigm reconciles the macroscopic compositional dishomogeneities observed in comets, as BPs, with the structural homogeneity at small (cm) scale of a nucleus made of pebbles, and with the processes at the base of water-driven activity at microscopic (sub-pebble) scales. The presence of sub-metre-sized WEBs indicates these are likely primordial: their origin as the recent product of orbital water-ice re-condensation processes within the nucleus seems unlikely[5], as these processes can be active only within very shallow depths[8,19]. At the same time, WEBs challenge the present comet formation

models, which would be required to explain primordial macroscopic localisation of water ice (although mainly at sub-metre scale rather than tens of metres) in the material forming cometary nuclei.

Proto Planetary Disk (PPD) observations[46] have shown segregation of dust grains populations with or without a water-ice mantle but also the presence of icy dust grain clouds intermixed with ice-poor grains, which implies the presence of water-ice-rich and water-ice-poor pebbles. The detection of crystalline water ice in PPDs[47] suggests the occurrence of localised re-condensation processes from the ISM to PPDs (in e.g. hot-corinos[41]), that may lead to the formation of water-ice-rich grains. The complex evolution of the PPD led to the formation of water-ice-rich and water-ice-poor pebbles in different regions of the PPD[46], followed by mixing processes[47]. Water-ice-rich pebbles are stickier than water-ice-poor ones, and this could favour the formation of WEBs during the gravitational collapse, generated by a streaming instability process of clouds of pebbles that formed comets[12].

Methods

Condition for water-driven activity

According to the cometary activity model for a nucleus made of pebbles by ref.[10], dust emission upon water ice sublimation (water-driven erosion) can be described by means of two characteristic rates, represented by the dust erosion rate $E(T)$ and the dehydration rate $D(T)$, both depending on the surface temperature T. The former represents the thickness of the surface layer eroded into dust per unit time, while the latter is the thickness of the surface layer which gets dehydrated by water ice sublimation per unit time. The condition for a given area to be active is that $E(T) \geq D(T)$. If not, in the surface upper layer dehydration occurs more rapidly than erosion, developing a dry and insulating crust which prevents further activity if not refreshed by CO_2-driven erosion[10]. From ref.[10] the dehydration rate can be expressed as

$$D(T) = (\delta + 1)\frac{Q_g(T)}{\rho_n}. \tag{1}$$

where $Q_g(T)$ is the gas emission rate and $\rho_n = 538$ kg/m^3 is the nucleus density[48]. Unlike the dehydration rate, the erosion does not depend on the dust-to-water-ice mass ratio δ, and we refer the reader to ref.[10] for the expression of $E(T)$. Positing $D(T) = E(T)$ we obtain from Eq. 1 the maximum value of δ (δ_{MAX}) for which the surface can be active, which is a function of the surface temperature T:

$$\delta_{MAX}(T) = \rho_n \frac{E(T)}{Q(T)} - 1. \tag{2}$$

By taking into account the insolation history of the Imhotep ROI (Fig. 5), we estimate the temporal evolution of the corresponding maximum surface temperature as provided by the model of ref.[10] and obtain $\delta_{MAX}(T)$ at different times from Eq. 2 (Fig. 6). In general, δ_{MAX} decreases with increasing temperatures, and for the Imhotep ROI it attains its minimum around perihelion. With the same approach it can be shown that in August 2014 the Hapi region is active if $\delta < 10^3$, while $\delta < 5$ is required for the southern hemisphere at perihelion[10].

Modelling of BP temporal variability

Explaining the colour variability of a cometary nucleus as the effect of the progressive exposure of new BPs from CO_2-driven activity implies a distribution of discrete subsurface Water-Ice-Enriched Blocks across the whole comet. The WEBs are exposed by the removal of overlying chunks lifted by CO_2 sublimation[11]. The exposed parts of the WEBs appear as BPs on the surface, and their abundance at a

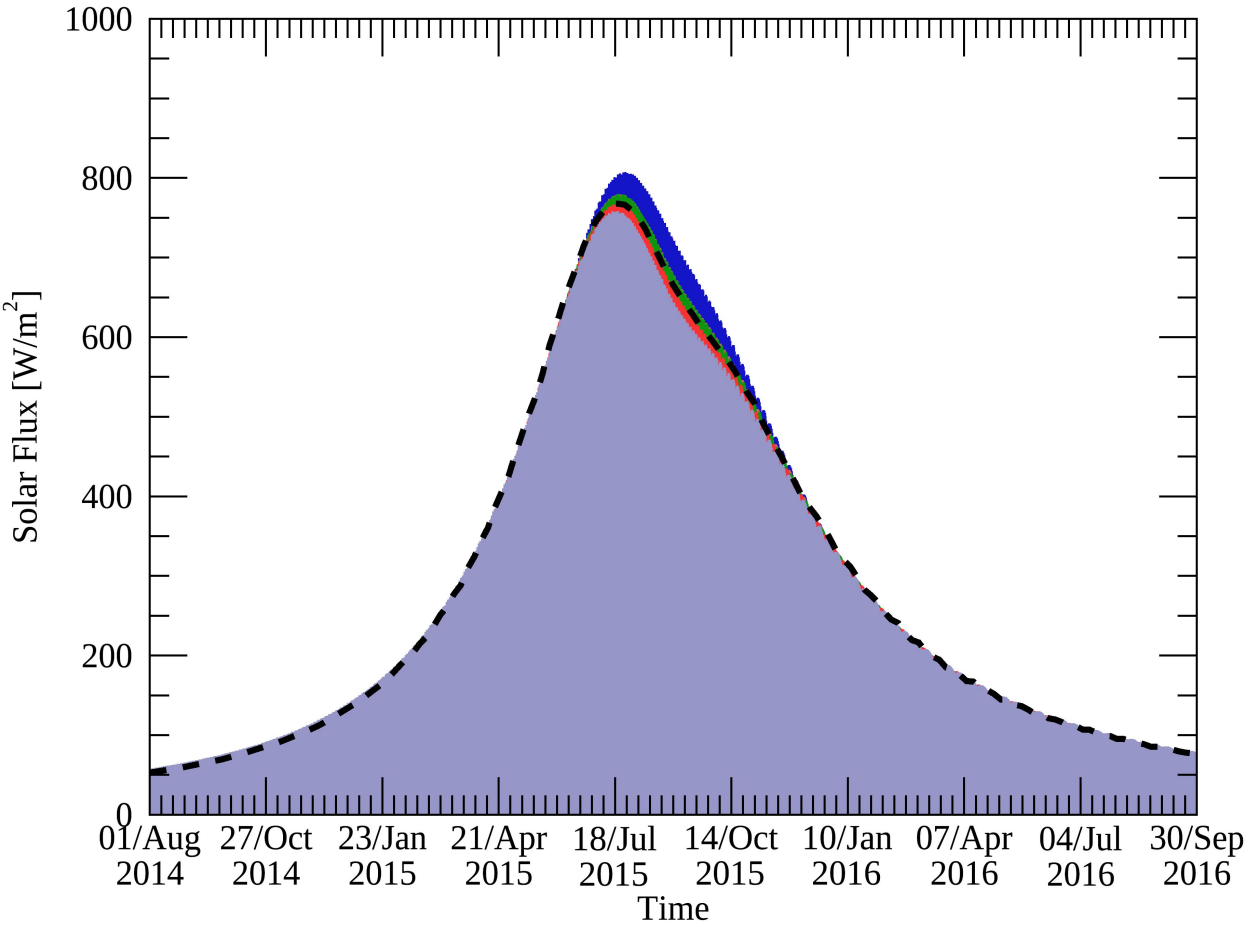

Figure 5. Insolation over the Imhotep ROI. The incident solar flux at the surface from August 2014 to September 2016 has been computed at five positions, corresponding to the ROI corners and centre by means of the SPICE tool[49]. This result in five different curves that are superimposed in the plot (as a consequence only four of them are visible). The insolation curves account also for the diurnal cycle on the comet surface, thus, in a single rotation the Solar flux on the Imhotep ROI is zero at night and maximum at noon. Note that in the present visualisation such day-night variability is not resolved. The curves of the five positions have been averaged to produce an average insolation curve of the Imhotep ROI (not shown). We report, as a black dashed line, the upper envelope of this curve, computed over a running box of approximately 10 comet rotations, representing the temporal evolution of the maximum flux over the Imhotep ROI.

given time results from the combined effect of CO_2-driven activity, which determines the BP exposure rate, and water ice sublimation, which erodes the BPs. We assume all the WEBs have $\delta < 5$, which ensures they can sustain water-driven activity up to perihelion. Both CO_2-activity and water ice sublimation are modulated by the surface temperature, which varies with time, and determine the temporal evolution of the BP abundance on the surface.

We assume that at the onset of the CO_2 activity, when the nucleus exhibits the maximum redness, the

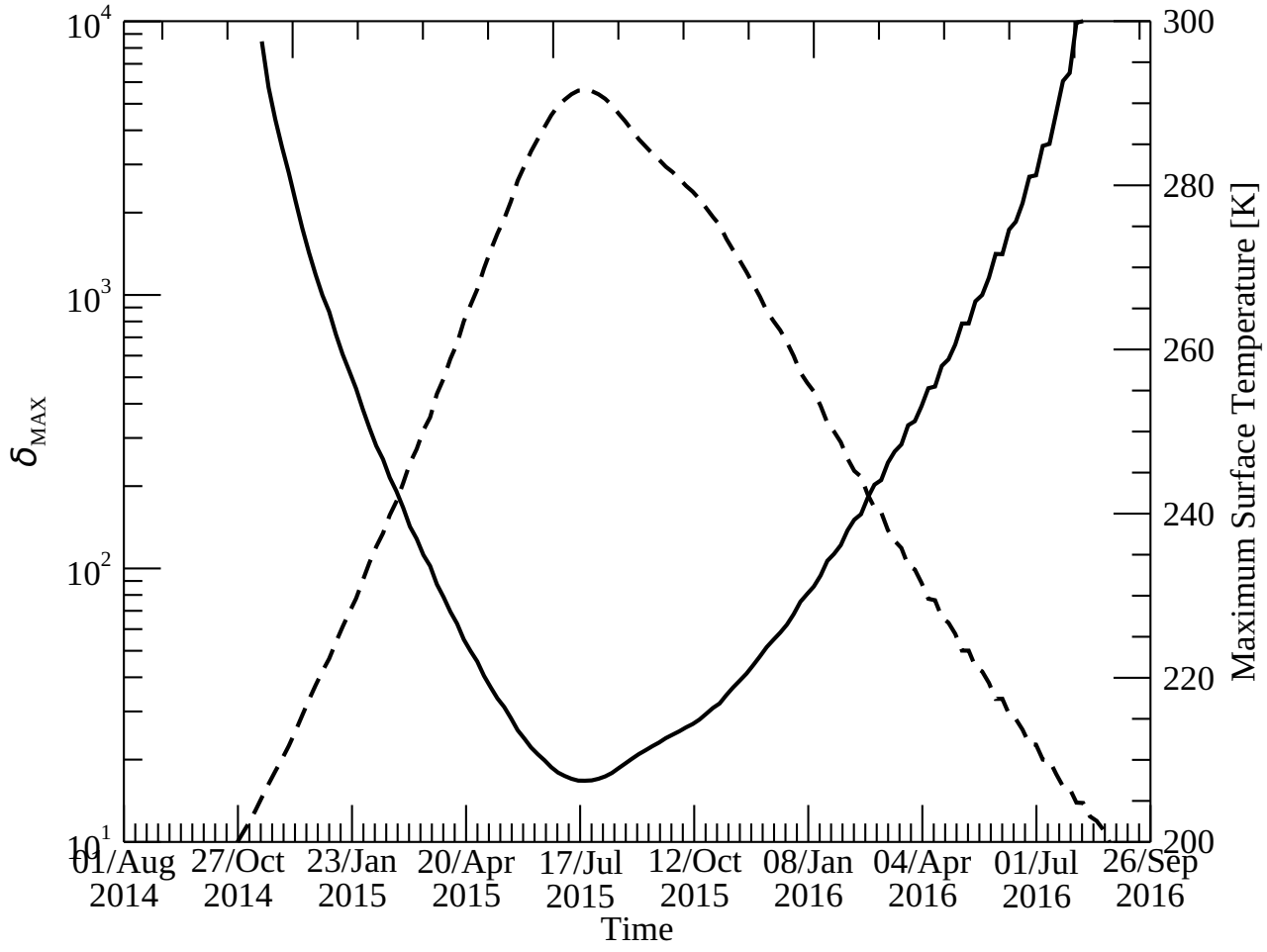

Figure 6. δ_{MAX} **and maximum surface temperature from August 2014 to September 2016 for the Imhotep ROI.** δ_{MAX} (solid line) is not defined before November 2014 and approximately after August 2016, as surface temperature in the Imhotep ROI is < 205 K and cannot sustain water-driven activity[10].The maximum surface temperature (dashed line) is computed from August 2014 to September 2016 by assuming the maximum solar flux over the Imhotep ROI shown in Fig. 5.

surface of the comet is characterised by a dehydrated layer covering an internal distribution of WEBs having a constant density with depth. For simplicity, we assume that the emission of a chunk from CO_2 sublimation in the dehydrated layer directly sample depths which are already representative of the internal density of WEBs. Depending on the numerical density of WEBs and their size, it is then possible to define the fractional area of WEBs in the subsurface, f_{WEB}, which represents the probability to expose a BP resulting from chunk emission. f_{WEB} also represents the WEB volumetric abundance in the nucleus. Let's now define $BP(t)$ as the fraction of the surface covered by BPs at the time t. At a given time, it is possible to express the variation of the areal fraction covered in BPs as

$$dBP(t) = dBP_{exp}(t) - dBP_{rem}(t), \tag{3}$$

where dBP_{exp}(t) is the increase in areal fraction of exposed BPs in the interval $[t, t+dt]$ due to CO_2-driven chunk emission and $-dBP_{rem}$(t) is the decrease of areal fraction due to BP removal produced by H_2O-driven and CO_2-driven erosion taking place over the BPs. Assuming $f_{CO2}(t)$ is the areal erosion rate from CO_2 activity (i. e. the areal fraction experiencing chunk emission), we can express dBP_{exp}(t) as

$$dBP_{exp}(t) = f_{CO_2}(t)(f_{WEB} - BP(t))dt, \tag{4}$$

where the term $-f_{CO_2}(t)BP(t)$ accounts for chunk emission taking place over already existing BPs, which does not increase the areal fraction of exposed WEBs.

The term $dBP_{rem}(t)$, accounts primarily for the sublimation of the exposed BPs. A BP sublimates completely after a time $\Delta(t)$ since the start of exposure, which depends on the H_2O-driven erosion rate and the WEB size L. In addition, CO_2 chunks emission may in principle take place also over exposed BP, which contributes to reducing their survival time. Given this, $dBP_{rem}(t)$ can be expressed as:

$$dBP_{rem}(t) = dBP_{exp}(t') = f_{CO_2}(t')(f_{WEB} - BP(t'))dt', \tag{5}$$

where $dBP_{exp}(t')$ is the areal fractional of BPs exposed in the interval $[t', t'+dt']$, with $t' = t - \Delta(t)$ and with $\Delta(t)$ being the time required to remove at time tf a BP first exposed at time t', due to erosion from water ice sublimation and CO_2 activity. The emission of chunks from CO_2 activity, which decreases the depth L of a given BP, by the typical chunk size, L_c, reduces also its sublimation time. Taking this into account, we define an effective depth $L_{eff}(t)$ of the BPs as follows:

$$L_{eff}(t) = L - L_c \times \int_{t'}^{t} f_{CO_2}(t^*)dt^*, \tag{6}$$

which represents the residual average depth of BPs exposed at time t', and where the term $L_c \times \int_{t'}^{t} f_{CO_2}(t^*)dt^*$ is the average depth eroded by CO_2-activity. Finally, $\Delta(t)$ is given by the implicit relation

$$L_{eff}(t) = \int_{t-\Delta(t)}^{t} E(t^*)dt^*, \tag{7}$$

where $E(t)$ is the erosion rate from water-ice activity in a BP.

For given values of L, f_{WEB} and L_c, the set of equations from Eq. 3 to Eq. 7 can be solved numerically, once $f_{CO_2}(t)$ and $E(t)$ are provided. For the Imhotep ROI, $E(t)$ can be determined from[10], by taking into account the insolation history of the region as reported in Fig. 5. We compute the average erosion rate with a 10-day running box and obtain the result of Fig. 7.

The quantity $f_{CO_2}(t)$ depends on the vertical erosion rate from CO_2-driven activity. To our knowledge, this has been modelled so far only for the southern hemisphere at perihelion[11]. Given this, for the purpose of this work, we test different formulations of $f_{CO_2}(t)$ computed starting from the H_2O-driven erosion rate $E(t)$, with the parametric expression $f_{CO_2}(t) = K\frac{E(t)^\alpha}{MAX(E(t)^\alpha)}$, where K is the areal erosion rate at maximum activity. This appears as a reasonable approximation, as $f_{CO_2}(t)$, like $E(t)$, is expected to be driven by the insolation conditions, being maximum around perihelion and decreasing monotonically with heliocentric distance.

Below, we report typical behaviors of the temporal evolution of the BP areal fraction $BP(t)$, for different values of α (Fig. 8). It can be noted that the $\alpha = 1$ case, after an initial transient phase, reaches a stationary regime. The transient phase ends with a local maximum well before perihelion, which is determined by the BP areal fraction build up due to the exposure of the first WEBs in November 2014 up to February-early

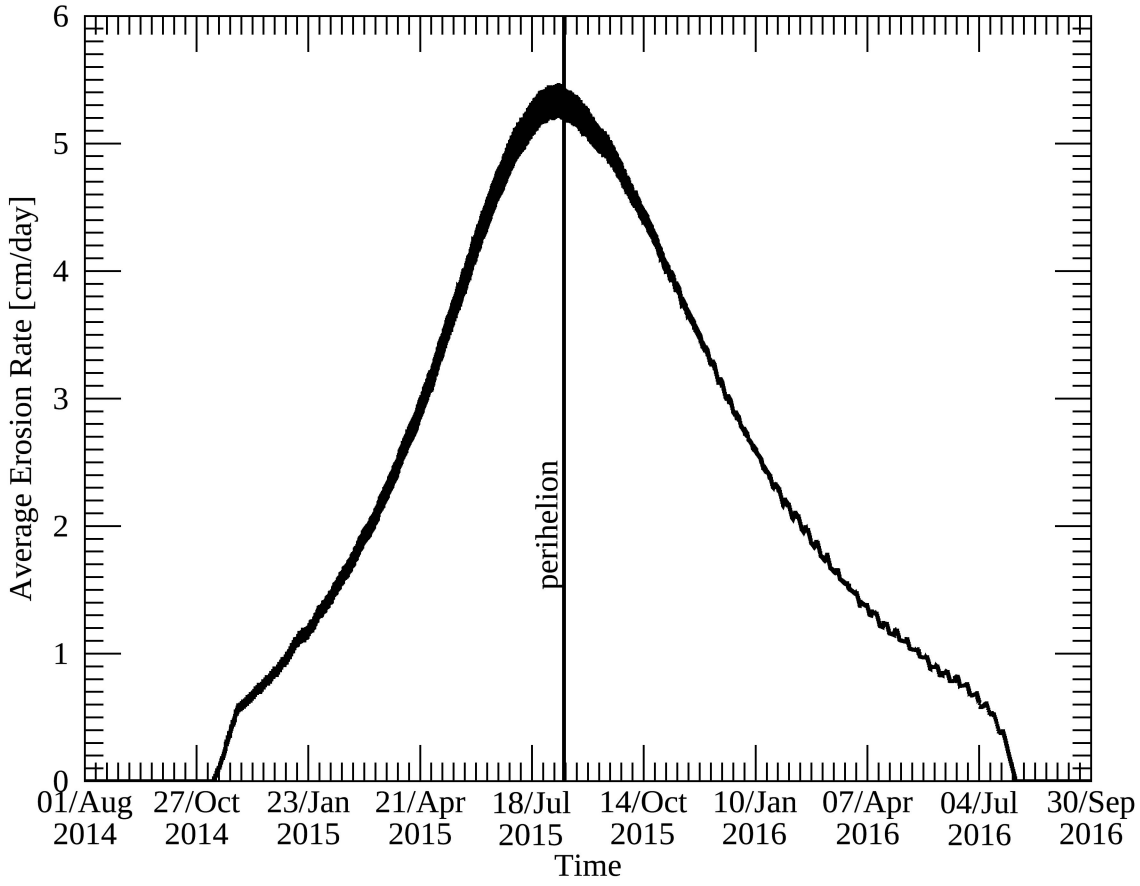

Figure 7. Average erosion rate in the Imhotep ROI. The curve is obtained after averaging over a 10-day running box.

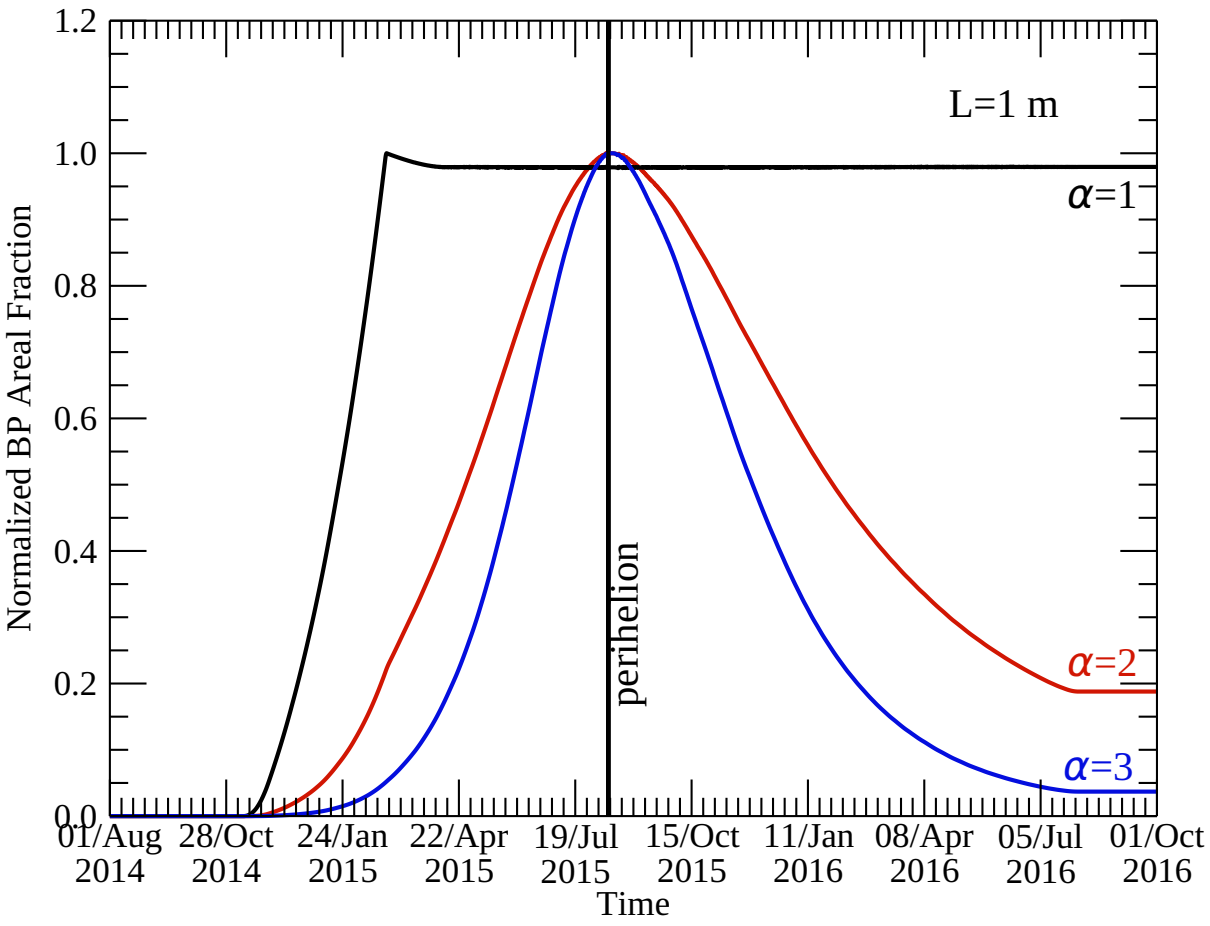

Figure 8. Temporal evolution of the BP areal fraction for different values of α. The normalized BP areal fraction is reported versus time, for different behaviors of f_{CO_2} as a function of the index α. For each simulation we adopted $f_{WEB} = 0.5$ and $K = 0.0001$ h^{-1} and WEB size $L = 1$ m and $L_c = 0.1$ m[11]. Such values allow the simulations to be far from a saturation regime, with maximum values of $BP(t) \ll f_{WEB}$.

March 2015, when the first BPs were be completely eroded. This build-up behaviour can be noted also for the $\alpha = 2$ case, while for $\alpha = 3$ it is less evident as the end of the transient regime occurs at low BP areal fractions. As the end of the transient phase depends on the sublimation time of the WEBs, it occurs earlier for smaller L (see the set of simulations for different Ls shown in Fig. 10, where the end of the transient phase appears shifting in time with the WEB size).
On the other hand, the occurrence of the stationary regime can be explained with the following reasoning. In the stationary condition we have $dBP_{exp}(t) - dBP_{rem}(t) = 0$. Assuming the areal coverage of BPs is far from saturation (i. e. the areal fraction of exposed BPs is much smaller than the areal fraction f_{WEB} in the interior of the comet, $BP(t) \ll f_{WEB}$), the stationary condition implies $f_{CO_2}(t) f_{WEB} dt = f_{CO_2}(t') f_{WEB} dt'$. In the time interval $[t, t+dt]$ BPs exposed in the interval $[t', t'+dt']$ finally sublimate. Then, in a regime of BP erosion dominated by water ice, we have

$$L = \int_{t'}^{t} E(t^*)dt^* = \int_{t'+dt'}^{t+dt} E(t^*)dt^* \tag{8}$$

which implies

$$\int_{t'}^{t'+dt'} E(t^*)dt^* = \int_{t}^{t+dt} E(t^*)dt^* \tag{9}$$

and finally $E(t')dt' = E(t)dt$. Given this, the stationary condition becomes $f_{CO_2}(t) f_{WEB} dt = \frac{f_{CO_2}(t')}{E(t')} f_{WEB} E(t) dt$. If $f_{CO_2}(t) \propto E(t)^\alpha$ we obtain $\frac{E(t)^\alpha}{E(t)} = \frac{E(t')^\alpha}{E(t')}$ which is trivially valid for every t and t' if $\alpha = 1$.
Conversely, if $\alpha \neq 1$, the stationary points of $BP(t)$ must satisfy $E(t)^{\alpha-1} = E(t')^{\alpha-1}$.

Position of the maximum of BP(t)

If $E(t)$ is characterised by a local maximum at t_{MAX}, as in the investigated case, and $alpha \neq 1$, the condition $E(t)^{\alpha-1} = E(t')^{\alpha-1}$ can be met for a certain combination of t, t', with $t > t_{MAX}$ and $t' < t_{MAX}$. Assuming that in the neighborhood of t_{MAX} the BP sublimation time is approximately constant $\Delta(t) \approx \Delta(t_{MAX})$ we have $dt' \approx dt$. Given this, expanding both $E(t)^{\alpha-1}$ and $E(t')^{\alpha-1}$ around t_{MAX} we obtain

$$E(t)^{\alpha-1} = E(t_{MAX})^{\alpha-1} + \frac{1}{2}\frac{d^2(E(t_{MAX})^{\alpha-1})}{dt^2} * (t - t_{MAX})^2 \tag{10}$$

$$E(t')^{\alpha-1} = E(t_{MAX})^{\alpha-1} + \frac{1}{2}\frac{d^2(E(t_{MAX})^{\alpha-1})}{dt^2} * (t' - t_{MAX})^2 \tag{11}$$

as $\frac{d(E(t_{MAX})^{\alpha-1})}{dt} = 0$ and where it can be shown that $\frac{d^2(E(t_{MAX})^{\alpha-1})}{dt^2} = (\alpha-1)E(t_{MAX})^{\alpha-2}\frac{d^2(E(t_{MAX}))}{dt^2}$. This is equivalent to

$$(t - t_{MAX})^2 = (t' - t_{MAX})^2 \tag{12}$$

which is the case

$$t = t_{MAX} + \Delta/2 \approx t_{MAX} + \frac{L}{2E(t_{MAX})}. \tag{13}$$

Interestingly, since t_{MAX} is the position of a local maximum, we have $\frac{d^2E(t_{MAX})}{dt^2} < 0$, that, for $\alpha > 1$, provides the stationary point $t = t_{MAX} + \Delta/2$ being the position of a local maximum of $BP(t)$, while for $\alpha < 1$ it identifies a local minimum. Given this, for the study of 67P's BP temporal evolution, only cases with

$\alpha > 1$ are of interest. The discussion above indicates that the maximum of $BP(t)$ is delayed with respect to the maximum of CO_2 activity by an amount that depends on the sublimation time of the BPs, and that is related to the size L of the WEBs. Thus, the quantification of such delay from the $BP(t)$ curve inferred from VIRTIS data would in principle provide an estimate of the WEB size. Assuming $\alpha = 2$, below we illustrate the effect on the final shape of $BP(t)$ for different sizes of the WEB (Fig. 9) by integrating numerically our set of equations. It is worth noting that if the condition $BP(t) \ll f_{WEB}$ is not met, i.e. the areal fraction of BPs is close to saturation, the considerations made above are not necessarily valid, and the position of the maximum of $BP(t)$ can be shifted at times $< t_{MAX} + \Delta/2$, preventing the determination of the WEB size from the position of the $BP(t)$ maximum (see also below).

Matching the BPs' temporal evolution for the Imhotep ROI

The set of equations described above is applied to model the temporal evolution of the BP abundance in the Imhotep ROI. For simplicity, we assume $\alpha = 2$ (as shown above, only cases with $\alpha > 1$ are of interest for 67P's BP temporal evolution) and investigate four different WEB sizes $L = 0.1, 0.5, 1, 2$ m. As described above, along with L and α, the model also depends on the three additional parameters L_c, K, and f_{WEB}. The chunk size L_c, determined by the depth of the CO_2 sublimation front, may vary with the heliocentric distance. However, here we adopt a constant value of $L_c = 0.1$ m which is comparable to values for the southern hemisphere at perihelion[11]. In this respect, a time-dependent formulation of L_c does not appear as strictly necessary, given the modelling uncertainty on $f_{CO_2}(t)$. Moreover, the adopted value of L_c is representative for the perihelion phase, where most of the CO_2-driven erosion takes place. The maximum areal erosion rate from CO_2 activity K can be fixed by taking into account the total vertical erosion measured in the Imhotep ROI. For the Imhotep region, the upper limit on the total erosion is 0.5 m, as determined by analysis of OSIRIS images[42]. According to this, we set our simulations to provide an erosion of ≈ 0.4 m through CO_2 erosion, which means requiring $L_c * \int_{Aug2014}^{Sept2016} f_{CO2}(t)dt \approx 0.4$ m. We verified that such value of CO_2-driven erosion is compatible with a total erosion of ≈ 0.5 m, when accounting for the water-ice-driven erosion in the BPs. For $\alpha = 2$, this condition fixes $K = 0.0262$ day^{-1} in our model, and by consequence the $BP(t)$ curve can be matched by varying the free parameter f_{WEB}. Such value of K results in a maximum CO_2-driven erosion rate at perihelion $K * L_c$ =0.262 cm/day, much smaller than the maximum water-driven erosion rate of 5.5 cm/day in the BPs. In Fig. 10 we report fits of the $BP(t)$ curve for the Imhotep ROI from VIRTIS data with the results of our simulations.

As post-perihelion fall-out of dehydrated material emitted around perihelion[44] may cover exposed BPs, stop water-driven erosion, and reduce the resulting abundance of BPs on the surface (see Supplementary material), the fit is performed by matching only the $BP(t)$ curve up to one month after perihelion, where the maximum blueing is measured. A good match of the BP curve can be achieved for $\alpha = 2$ with basically all the explored values of L. In particular, the simulations indicate that the smaller the size of the WEBs, the larger the f_{WEB} required to match the $BP(t)$ curve. This is explained by the fact that smaller WEBs sublimate faster, and then a larger abundance in the subsurface is required to sustain the increase of exposed BPs at perihelion. All the simulations peak close to perihelion, while the maximum on the $BP(t)$ curve for the Imhotep ROI appears shifted at one month after perihelion. However, given the error bars on the $BP(t)$ curve, and the coarse temporal resolution of the measured $BP(t)$ curve (30 days), we cannot consider such one month shift as diagnostic of the WEB size. In this respect, we note that the spectral-slope curve of the ROI E shows the maximum blueing slightly before perihelion, while ROI D displays a broader spectral-slope minimum centred at perihelion (Fig. 3). This is indicative of the uncertainty associated with the position at which maximum blueing occurs. It is worth noting that also the simulations performed with a large WEB size ($L = 2$ m, Fig. 10d), for which a significant shift of the BP maximum towards larger times after perihelion can be expected, still peak close to perihelion. This is explained by the fact that

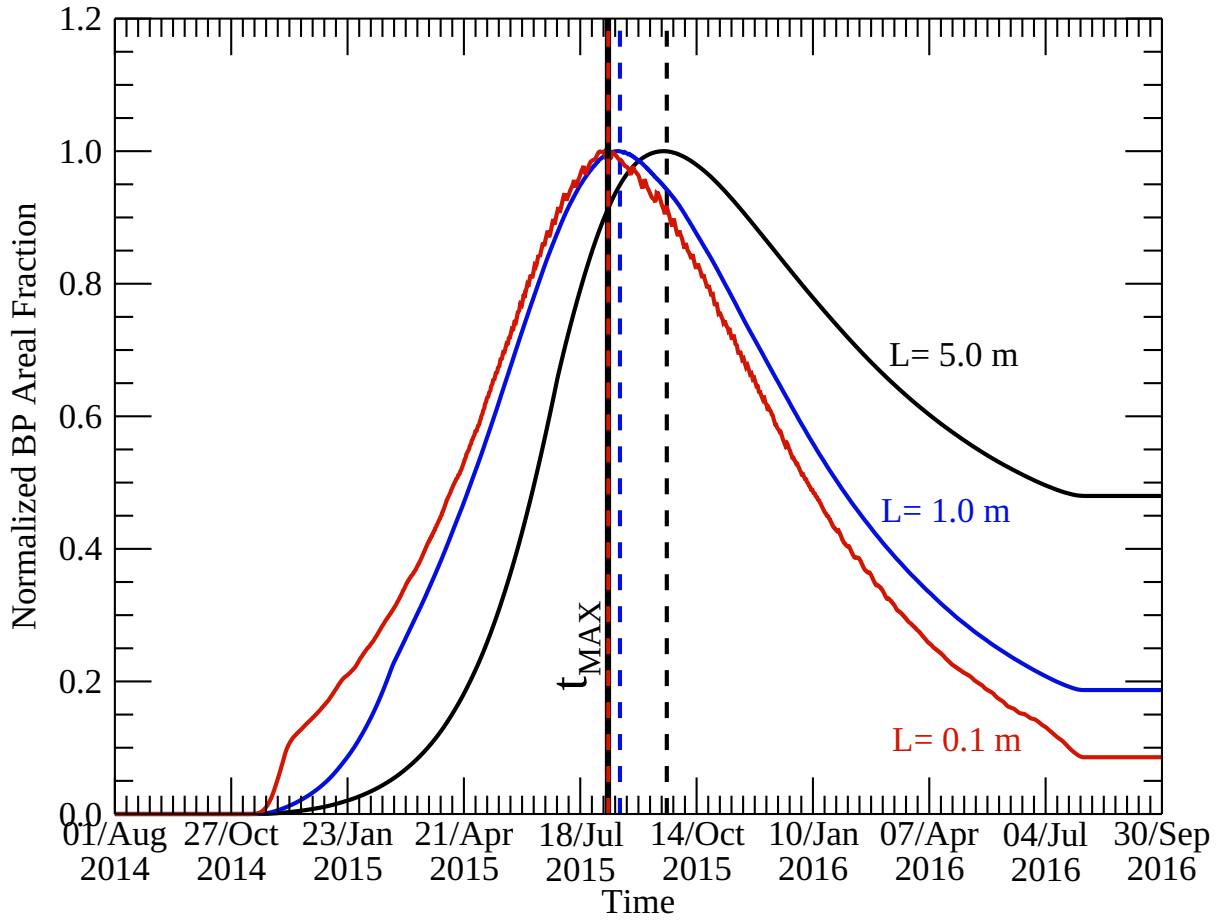

Figure 9. Normalized $BP(t)$ curves for different values of L. In these simulations we adopted $L_c \ll L$, $K = 0.0001$ h^{-1} and $f_{WEB} = 0.5$. For illustrative purposes, the selected values of L_c and K are chosen to provide a negligible effect of the additional erosion of the BPs from CO_2 activity. The positions of the local maxima for the different cases are indicated by dashed lines. The position of t_{MAX} is indicated with a solid line. The derived delay of the $BP(t)$ maximum with respect to the maximum in the activity is ≈ 1.5 days, ≈ 10 days and ≈ 46 days for $L = 0.1$ m, $L = 1$ m and $L = 5$ m, respectively. The delays, as estimated with Eq. 13 and $E(t_{MAX}) = 5.5$ cm/day are ≈ 0.9 days, ≈ 9 days and ≈ 46 days, in good agreement with the results from the numerical integration for $L = 0.1$ m, $L = 1$ m and $L = 5$ m, respectively. All the curves reach a plateau at the end of the investigated time interval. These correspond to the stop of water-driven erosion ($E(t) = 0$), which preserves the residual BPs in the simulation. However, in this regime, water ice sublimation, although not able to erode the surface, would cause dehydration of BPs[10], which eventually disappear. This effect is not included in the present model.

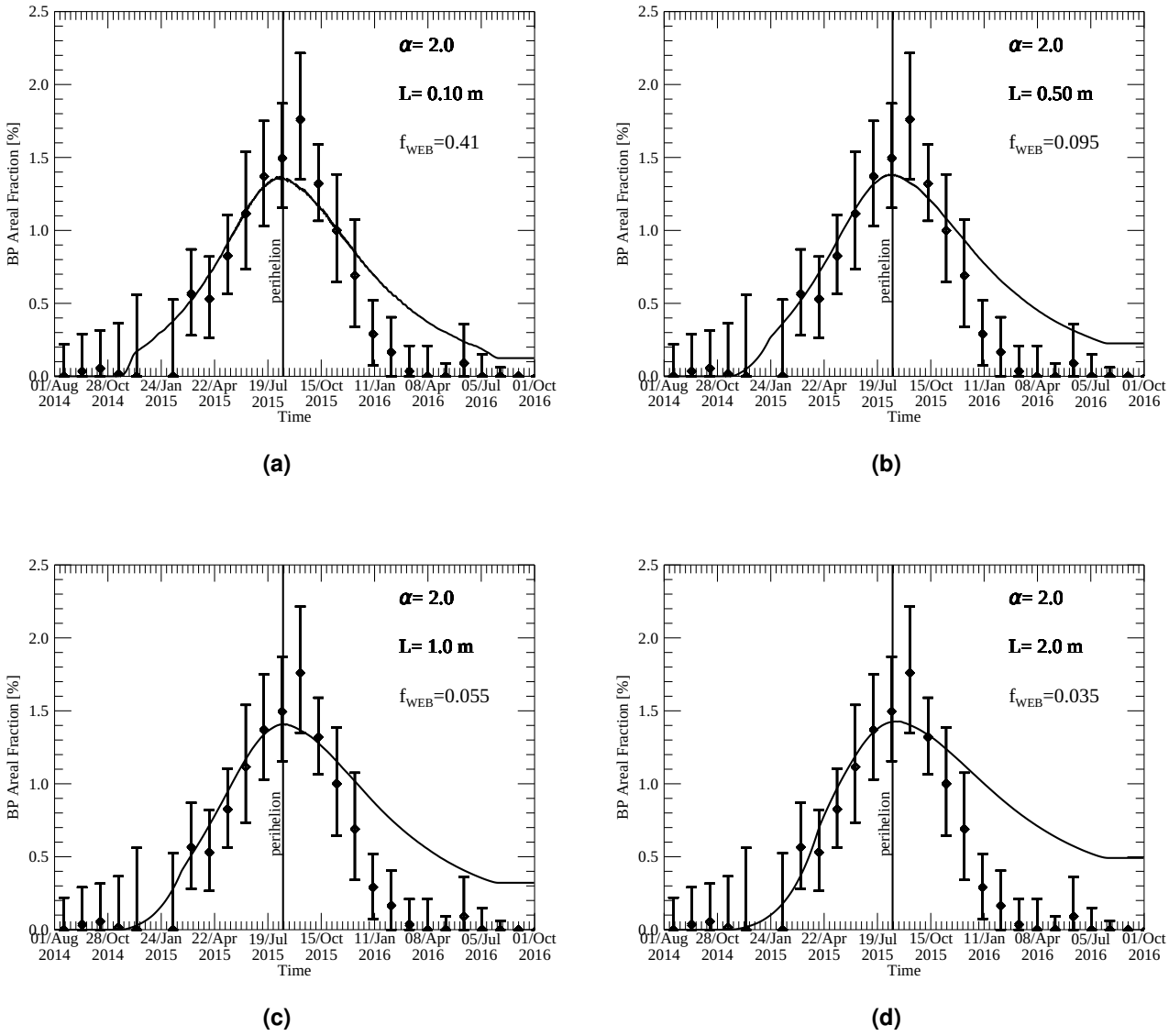

Figure 10. Best fit models of the BP temporal evolution over the Imhotep ROI. The BP areal fraction as derived from VIRTIS data (diamonds) is compared with models (solid lines) for L=0.1,0.5,1 ,2 m and α=2. The best fit values of f_{WEB} are reported.

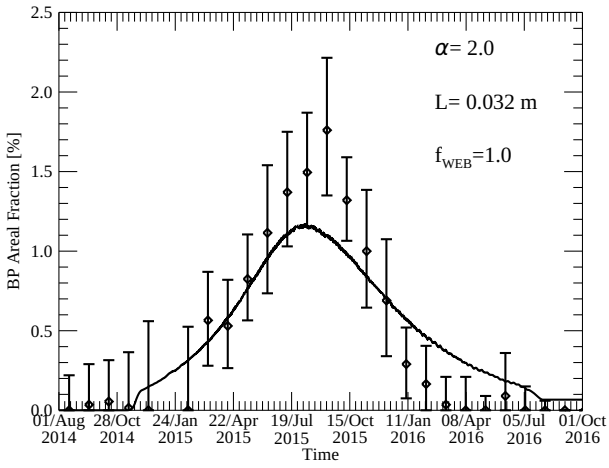

Figure 11. Characterisation of the WEB size lower limit. The temporal evolution of the BPs over the Imhotep ROI is compared with an ideal model assuming $f_{WEB} = 1$ and $\alpha = 2$. The value of L is chosen as the smallest one for which the obtained evolution of $BP(t)$ is still considered compatible with observations.

the required values of f_{WEB} are close to the maximum value of the BP curve, thus indicating that the BP abundance on the surface was approaching a saturation regime, in which case Eq. 13 cannot be directly applied.

Conversely, simulations run with $L = 0.1$ m (Fig. 10a)provide $f_{WEB} \approx 0.4$, much larger than the maximum value registered in $BP(t)$, which is of the order of $\approx 2\%$. As f_{WEB} increases with decreasing WEBs size, it is then possible to define a limit size of the WEBs for which $f_{WEB} = 1$ is required to match the BP temporal evolution in the Imhotep ROI. This would represent a lower limit of the typical size of the WEBs for comet 67P. In this regime, where $L_c > L$, the emission of a chunk removes the BPs present in its area and simultaneously exposes new WEBs below. In this case, f_{WEB} represents the average areal fraction of BPs at the scale of the area exposed by the chunk emission $\approx {L_c}^2$. To treat this case we slightly simplify our model, by neglecting the term $BP(t) \ll f_{WEB}$ in Eqs. 4 and 5, and setting $L_{eff}(t) = L$, since in this regime, exposed BPs can be eroded by water ice sublimation only. In Fig. 11 we show the result of a simulation with $\alpha = 2$ and the smallest values of L (L_{min}) for which the observed trend is still matched. We obtain that the simulated temporal evolution of BPs on the surface is still compatible with the observed one if $L_{min} = 0.032$ m. Smaller values of L would not be able to match the temporal evolution in Imhotep, and as a consequence L_{min} provides an estimate of the lower limit of the WEB size. We also stress that in the ideal limit $f_{WEB} = 1$, WEBs would no longer be separate units with a finite size. Thus, the provided value of L_{min} represents the asymptotic WEB size in this regime and underestimates the physical WEB size lower limit.

In addition, also an upper limit for the WEB size can be provided. In May 2015, when VIRTIS already measured a detectable blueing in the Imhotep ROI, OSIRIS Narrow Angle Camera (NAC) observations with a nominal spatial resolution of 2.4 m/pixel show a significant blueing over an extended area in the central part of the Imhotep region[8]. Considering a reference point spread function FWHM for the OSIRIS NAC of $\approx$1.8 pixels[50,51], we can conclude that BPs are almost evenly distributed over a spatial scale of 2.4×1.8 m$= 4.32$ m in this region. This implies that each surface element corresponding to the equivalent OSIRIS pixel, having an area $A_{eq} = (4.32\text{ m})^2 = 18.7\text{ m}^2$, approximately hosts the BP areal fraction observed by VIRTIS. This also indicates that roughly each surface element hosts at least one

WEB partially or fully exposed, depending on the size. As f_{WEB} represents the areal fraction of WEBs at depth, and assuming a uniform distribution of the WEBs in the subsurface, with a given size L, we have on average one WEB for each surface element of area $A = L^2/f_{WEB}$. In order to be compatible with the May 2015 OSIRIS NAC observations of the central part of the Imhotep region, A must be smaller than A_{eq}, thus granting that a large part of the equivalent pixels are populated by WEBs. For $L = 1$ m and the corresponding $f_{WEB} = 5.5\%$, as obtained by our simulations, we have $A \approx 18 - 19$ m^2. Given that A_{eq} represents a lower limit of the real projected area of the equivalent pixel (Nadir observation geometry), and OSIRIS spectral-slope images of this region are not fully uniform and show residual pixel-by-pixel variability, we can conclude that a WEB size of $L = 1$ m is compatible with OSIRIS observations. Larger WEB sizes require smaller values of f_{WEB} resulting in a larger A. For example, with $L = 2$ m and $f_{WEB} = 3.5\%$ we obtain $A \approx 114$ m$^2 > A_{eq}$. This indicates that $L \approx 1$ m is also a good estimate of the maximum WEB size. After May 2015, OSIRIS NAC observations have a nominal spatial resolution worse than 2 m/pixel roughly until mid-December 2015, when the BP abundance is characterised by values similar to May 2015. In later periods, the nominal spatial resolution of OSIRIS NAC observations is typically better than 2 m/pixel. However, the BP areal fraction rapidly reduces to ≈ 0 in early February 2016. This virtually prevents us to further constrain the WEB size upper limit with the approach described above, given the limited occurrence of BPs when OSIRIS NAC observes at better spatial resolution.

Supplementary Information

Period	MTP	Avg. heliocentric distance	Spatial resolution
1 August 2014 - 2 September 2014	MTP006	3.54 au	13-98 m/pixel
8 April 2015 - 5 May 2015	MTP015	1.83 au	23-39 m/pixel
25 August 2015 - 22 September 2015	MTP020	1.28 au	78-107 m/pixel
17 November 2015 - 15 December 2015	MTP023	1.78 au	25-36 m/pixel
31 May 2016 - 28 June 2016	MTP030	3.20 au	3-8 m/pixel

Table S1. Timing of the spectral-slope maps of Fig. 2. The corresponding Rosetta Medium Term Planning (MTP) phases are indicated, along with the comet average heliocentric distance and the spatial resolution of VIRTIS observations.

ROI	Latitude	Longitude	Morphological region
A	−30° – 0°	120° – 150°	Imhotep
B	15° – 30°	135° – 150°	Imhotep/Ash
C	−15° – 0°	255° – 270°	Hapi/Seth
D	0° – 10°	350° – 359°	Hatmehit
E	−75° – −60°	120° – 150°	Imhotep/Bes

Table S2. Latitude and longitude intervals of the ROIs defined in Fig. 2. The last column indicates the morphological regions where the ROIs are located, following the regional nomenclature from[27].

Spectral-slope computation and mapping

Maps of spectral slope are produced following the approach described in ref.[7] from photometrically reduced data[52], by converting the calibrated radiance factor ($I/F{=}\pi \times reflectance$) measured by VIRTIS-M nucleus observations into spectral single scattering albedo (SSA or w, Eq. 23)[53]. Such approach allows us to minimise the spectrophotometric effects induced by the variation of observation geometry on the surface reflectance and permits to compare acquisitions taken under different observation geometries and at different times. Following the method adopted in previous studies[7,22], for each SSA spectrum the spectral slope at visible wavelengths is computed as

$$S_{VIS} = \left(\frac{\Delta SSA}{\Delta\lambda}\right)_{0.55-0.8} \frac{100\%}{SSA_{0.55}}, \tag{14}$$

where $\left(\frac{\Delta SSA}{\Delta\lambda}\right)_{0.55-0.8}$ is the slope of a linear fit in the 0.55-0.8 μm interval, and $SSA_{0.55}$ is the single scattering albedo at 0.55 μm. Note that for the S_{VIS} computation we express wavelength in 100-nm unit, thus the S_{VIS} unit is %/(100 nm).

Correction of the effect of calibration residuals on S_{VIS}

VIRTIS-M observations are performed by acquiring sequences of *lines*, which correspond to images of the target through the spectrometer slit. The different *lines*, composed of 256 pixels (*samples*) each, are put together to produce the final VIRTIS-M bidimensional image at a given wavelength[24]. An analysis of the SSA spectral slope (S_{VIS}) from VIRTIS-M hyperspectral images (*cubes*), revealed two residual calibration issues which manifested as 1) a systematic correlation of S_{VIS} with the sample position (s) in

the VIS detector and 2) a positive correlation of S_{VIS} with the VIS detector (CCD) temperature. Below, we describe the empirical approach we adopted to correct the derived spectral slope in the visible for such effects.

Correction for S_{VIS} sample dependence

In order to model and then correct the observed dependence of S_{VIS} on the sample position (s) we selected six VIRTIS-M hyperspectral images (see Table S3) where the instrument FOV (field of view) was fully occupied by the nucleus and with limited occurrence of shadows. Each hyperspectral cube has been reduced to SSA (Eq. 23) and converted to a S_{VIS} image by computing the spectral slope for each pixel. For each image ι, a median $S^{\iota}_{VIS}(s)$ profile along the sample direction has been derived, by computing the median spectral-slope value for pixels corresponding to different lines at the same sample (Fig. S1b). Each of the different $S^{\iota}_{VIS}(s)$ median profiles has been normalised to its median value along the samples obtaining a Slope Correction Factor ($SCF^{\iota}(s)$) profile. Finally, the median of the $SCF^{\iota}(s)$ profiles from the different images have computed at each sample position to obtain a final slope correction factor $SCF(s)$ (Fig. S1c). With the aim to correct the derived spectral-slope images for the systematic dependence on the sample position, the derived value of the spectral slope at a given s is divided by the value of the $SCF(s)$ at the same sample (Fig. S1d).

Cube	Date	Number of lines	Target distance [km]
V1_00418865371	9 Apr 2016	202	28.2
V1_00430446438	22 Aug 2016	120	4.9
V1_00431457438	2 Sept 2016	63	4.2
V1_00431742197	6 Sept 2016	57	3.5
V1_00433297397	24 Sept 2016	58	3.9
V1_00433665027	28 Sept 2016	82	21.1

Table S3. List of the hyperspectral cubes selected to develop the S_{VIS} sample dependence correction, and corresponding observation circumstances.

Correction for S_{VIS} instrument temperature dependence

A comparison among VIRTIS-M spectral-slope images acquired in sequence evidenced that the average value of the spectral slope in each image is positively correlated with the VIS detector (CCD) temperature (also referred to as focal plane temperature) at the time of acquisition. Starting from the beginning of May 2015, corresponding to the end of the operations of the cryocooler used to cool down the IR detector, the VIS channel acquisition mode has been reconfigured to operate with longer integration and repetition times. This strategy has allowed the SNR of the VIS channel to be improved at expenses of a progressive warming of the CCD and higher operating temperatures, resulting in a systematic change of the detector response. In the following we report about the strategy used to correct this effect and homogenise the response across the entire dataset, an operation necessary to compare data collected during the entire duration of the mission. In Fig. S2 a sequence of images, acquired in ≈ 4.5 hours, with a single cube acquisition time of approximately 30 minutes, is shown. A clear increase of the measured spectral slope across the whole illuminated nucleus can be observed, from the first to the last acquisition, along with the focal plane temperature. In order to correct for this effect, a statistical approach has been developed to model the spurious increase of the measured spectral slope with temperature. To this purpose, we assume that, for a given acquisition, the effect of the corresponding CCD temperature (T) on the average of the computed spectral slope across the nucleus after photometric reduction, can be modelled by a

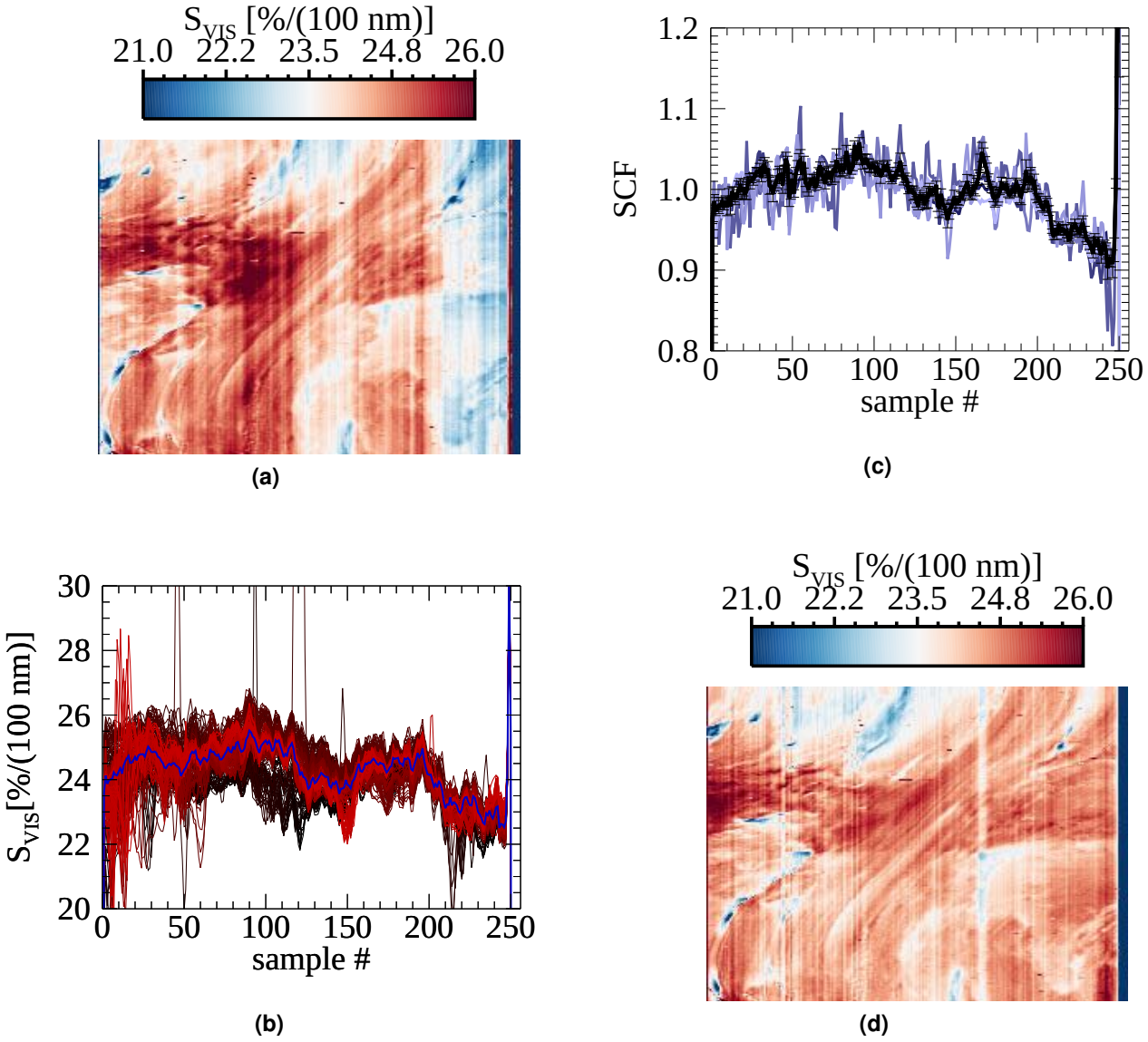

Figure S1. Characterisation and correction of the S_{VIS} sample dependence. a) S_{VIS} image as derived from VIRTIS-M hyperspectral cube V_00418865371. Surface features deformation is due to the spacecraft movement relative to the nucleus surface during acquisition. Notice the bluish band on the right side of the image corresponding to samples with systematically lower spectral slope. b) $S_{VIS}(s)$ profiles from each line of the image (curves with different red colour tones) and the corresponding median profile (blue thick curve). c) $SCF^{\prime}(s)$ profiles for each observation of Table S3 and median $SCF(s)$ (black thick curve) with formal errors. d) S_{VIS} image after the application of the Slope Correction Factor.

multiplicative term $f(T)$ according to the following relation

$$S_{VIS}(n,T) = S^{*}_{VIS}(n) \times f(T), \tag{15}$$

where the index n indicates the nth hyperspectral cube and $S^{*}_{VIS}(n)$ refers to the intrinsic average spectral slope of the surface. We assume that S^{*}_{VIS} is not correlated with the CCD temperature, then by averaging

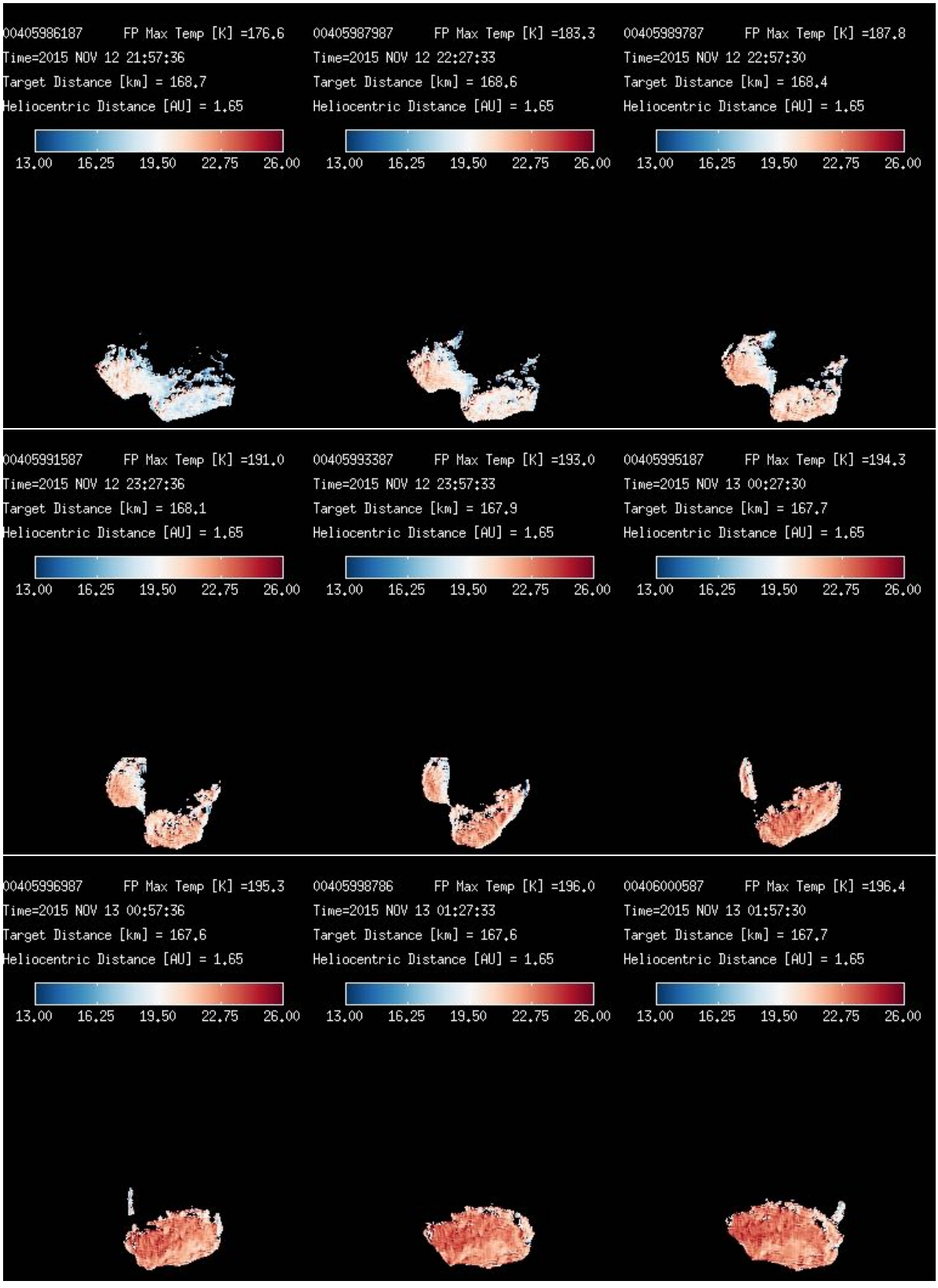

Figure S2. Effect of S_{VIS} dependence on the CCD temperature. Sequence of S_{VIS} images from cubes acquired between 12 and 13 November 2015. The acquisition of a single cube took approximately 30 minutes. Phase angle was $\approx 61^\circ$ for all the images, and additional observation circumstances are indicated. Between the first and the last acquisition, the instrument progressively warmed up and the maximum focal plane temperature (FP Max Temp), where the CCD is located, increased from 176.6 K to 196.4 K. This produced a systematic increase of S_{VIS} across the nucleus. Colour bar values are given in %/(100 nm).

over different images ($\langle\ \rangle_n$) for a given T, we obtain the following relation

$$\langle S_{VIS}(n,T)\rangle_n = \langle S^*_{VIS}(n)\rangle_n \times f(T). \tag{16}$$

Given that the instrument was calibrated at a nominal operating focal plane temperature of 180 K we can consider this temperature as the reference value at which the derived spectral slope is representative of the intrinsic properties of the nucleus. Then we can set $f(180\ \mathrm{K}) = 1$ which implies $S^*_{VIS}(n) = S_{VIS}(n, 180\ \mathrm{K})$ and

$$\langle S_{VIS}(n,T)\rangle_n = \langle S_{VIS}(n,180\ \mathrm{K})\rangle_n \times f(T), \tag{17}$$

where $\langle S_{VIS}(n,T)\rangle_n$ represents the average derived nucleus spectral slope as a function of the temperature (slope-temperature profile), that, for brevity of notation, we rename as $S_{VIS}(T)$. It follows that Eq. 17 can be now expressed as

$$S_{VIS}(T) = S_{VIS}(180\ \mathrm{K}) \times f(T) \tag{18}$$

which provides a general relation between the computed VIS spectral slope, its reference values at $T = 180$ K, and the CCD temperature T during the acquisition. To estimate $f(T)$ and $S_{VIS}(180\ \mathrm{K})$ in Eq. 18, a set of 10^6 slope-temperature profiles has been generated from VIRTIS-M observations acquired with different CCD temperatures in the 160 K<T<200 K range. The slope-temperature profiles have been built with a temperature sampling of $\Delta T = 1$ K by extracting randomly from the VIRTIS-M $S_{VIS}(n,T)$ distribution a value of the VIS spectral slope for each temperature bin. Observations are taken from Rosetta Medium Term Planning (MTP) sequences MTP017, MTP018, MTP022, MTP023, MTP024, MTP025, MTP026, MTP028 which were performed under variable CCD temperature conditions and sampled different phases of the comet surface evolution. The 10^6 spectral-slope profiles have been modeled with a linear fit where $f(T) = A + BT$. We note that according to Eq. 18 the quantities derived from the linear fit are actually given by $S_{VIS}(180\ \mathrm{K}) \times A$ and $S_{VIS}(180\ \mathrm{K}) \times B$, which will be referred to as SA and SB, respectively. By fitting the different 10^6 slope-temperature profiles a distribution for SA and SB is obtained, from which we derived the average values $SA = (-11.8 \pm 3.5)$ %/(100 nm) and $SB = (0.177 \pm 0.021$ %/(100 nm K). The final values for A, B, and $S_{VIS}(180\ \mathrm{K})$ are straightforwardly derived by imposing $f(180\ \mathrm{K}) = 1$. This gives $B = (1 - A)/(180\ \mathrm{K})$, from which it follows: $A = -0.5 \pm 0.17$, $B = (0.0088 \pm 0.00095)\ \mathrm{K}^{-1}$ and $S_{VIS}(180$ K$) = (20.001 \pm 0.028)$ %/(100 nm). In Fig. S3 we report the average of the 10^6 spectral-slope temperature profiles and Eq. 18 as computed with the estimated average values of SA and SB. It can be noted that the dependence of the computed spectral slope on the CCD temperature can be effectively described by a linear relation.

By using Eq. 18 and the results of the linear fit, the spectral slope for a given pixel $S^p_{VIS}(T)$ can be translated to its reference value at 180 K, $S^p_{VIS}(180\ \mathrm{K})$, by means of the simple relation $S^p_{VIS}(180$ K$) = (S^p_{VIS}(T))/f(T)$. In Fig. S4 we show the sequence of spectral-slope images of Fig. S2 after correcting for the CCD temperature dependence, demonstrating that the spurious increase of spectral slope with temperature has been properly corrected.

Spectral modelling

We describe the cometary surface as a geographical (or areal) mixture of the cometary dark terrain (being poor in water ice and having a low albedo) and BPs. The corresponding reflectance can then be expressed as a linear combination of the radiance factor of the dark terrain (I/F_{DT}) and of the BPs (I/F_{BP}):

$$I/F = (1 - f_{BP})I/F_{DT} + f_{BP}I/F_{BP}, \tag{19}$$

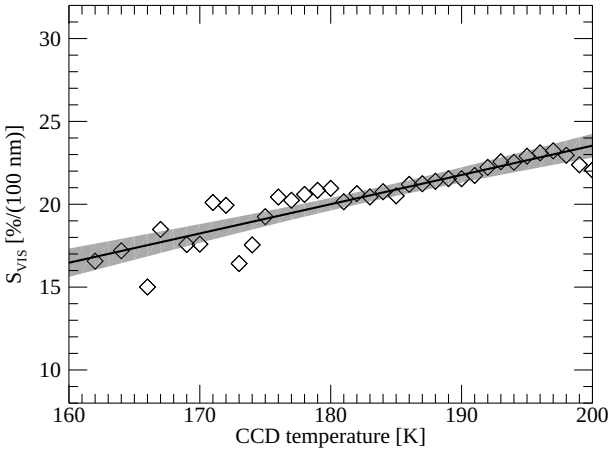

Figure S3. S_{VIS}**-CCD temperature average profile.** S_{VIS} and the CCD temperature are correlated and their relation has been fitted with the linear model (black curve) of Eq. 18 and $SA = -11.8$ %/(100 nm) and $SB = 0.177$ %/(100 nm K). We indicate as a grey band the 98% confidence interval for the predicted values in the linear regression: at 200 K the width of the confidence interval is ≈ 6% of the best fit value, and reduces to ≈ 4% at 180 K. These can be considered as conservative estimates of the error on the correction for the spectral-slope dependency on the CCD temperature.

where f_{BP} is the areal fraction of BPs. By applying a simplified version of the Hapke model[53] it has been shown[52] that, far from the opposition effect region, the dark terrain radiance factor for comet 67P can be expressed as

$$I/F_{DT} = \frac{w_{DT}(\lambda)}{4}\frac{\mu_{0e}}{\mu_{0e}+\mu_e}\Pi_{DT}(\lambda,g)S(i,e,g,\bar{\theta}), \tag{20}$$

where the contribution of multiple scattering is considered negligible given the low albedo of the surface, and with i,e,g being the incidence, emission and phase angles, respectively, μ_{0e} and μ_e the effective cosines of the incidence and emission angle, $w_{DT}(\lambda)$ the single scattering albedo of the dark terrain, $\Pi_{DT}(\lambda,g)$ the single particle phase function of the dark terrain and $S(i,e,g,\bar{\theta})$ the shadowing function of the surface, depending on the roughness parameter $\bar{\theta}$. Always referring to the Hapke theory, the radiance factor of the BPs can expressed as

$$I/F_{BP} = \frac{w_{BP}(\lambda)}{4}\frac{\mu_{0e}}{\mu_{0e}+\mu_e}[\Pi_{BP}(\lambda,g)+H(w_{BP},\mu_{0e})H(w_{BP},\mu_e)-1]S(i,e,g,\bar{\theta}), \tag{21}$$

where H is Chandrasekhar's function and accounts for multiple scattering. The BPs, similarly to the rest of the surface, are composed of pebbles. In the BPs, pebbles are agglomerates of cometary dark terrain and water ice, thus we model them as an intimate mixture of these two end-members. This implies that the BP single scattering albedo can be expressed as a linear combination of the dark terrain (w_{DT}) and water ice (w_I) single scattering albedos:

$$w_{BP} = f_I w_I + (1-f_I)w_{DT}, \tag{22}$$

where f_I is the ice fraction in the BPs. In our simulation we assume a reference value of $f_I = 0.5$, in line with the estimated dust-to-water-ice volume ratio of ice-rich features on comet 67P[5,37]. For the single

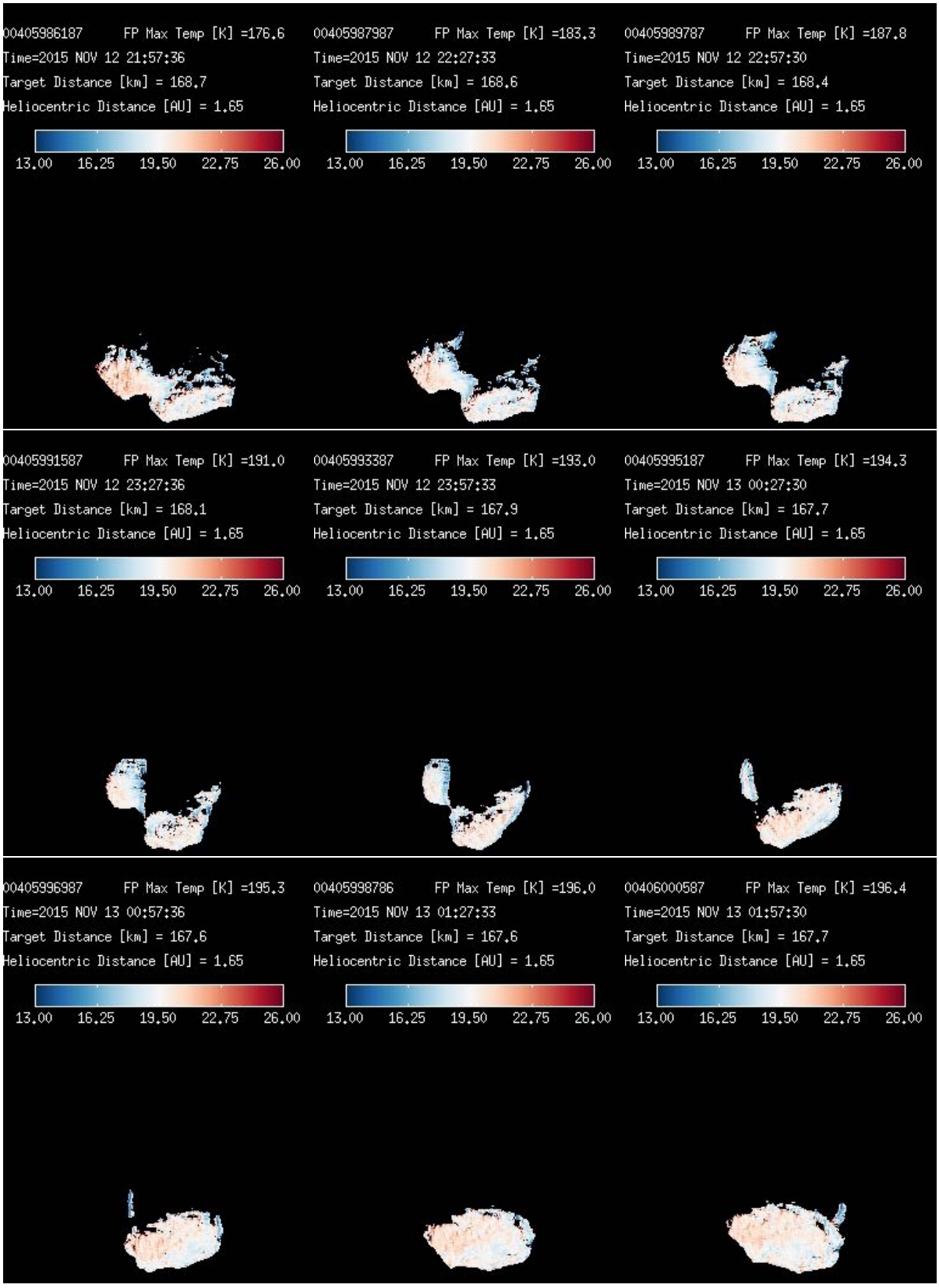

Figure S4. Correction of the S_{VIS} dependence on the CCD temperature. The same sequence of S_{VIS} images from Fig. S2, after correction for the CCD temperature effect on the computed spectral slope. Colour bar values are given in %/(100 nm).

scattering albedo of the comet's dark terrain we use the spectrum provided for the "bottom" region in ref.[52], while for the water ice case we assume a constant value of $w_I = 1$, which is an excellent approximation of the results obtained from Hapke's modelling of water ice grains in the 0.55-0.8 μm spectral range over a wide interval of grain sizes, from sub-μm- to mm-sized particles. As mentioned above, the spectral slope S_{VIS} has been derived after reduction of VIRTIS-M I/F measurements into single scattering albedo, which according to ref.[52] is provided by the following general equation

$$w(\lambda) = \frac{I/F_{VIRTIS}}{\Pi_{DT}(\lambda, g)} \frac{\mu_{0e} + \mu_e}{\mu_{0e}} \frac{4}{S(i, e, g, \bar{\theta})}. \tag{23}$$

Given this we apply Eqs. 19 to 23 to reduce the radiance factor of an ice-hosting area into the corresponding "effective single scattering albedo", w_{eff}, obtaining

$$w_{eff} = \Big((1 - f_{BP}) w_{DT}(\lambda) \Pi_{DT}(\lambda, g) + f_{BP}\big(w_{BP}(\lambda)[\Pi_{DT}(\lambda, g) + H(w_{BP}, \mu_{0e}) H(w_{BP}, \mu_e) - 1]\big)\Big) / \Pi_{DT}(\lambda, g), \tag{24}$$

where we assumed $\Pi_{BP} = \Pi_{DT}$ and Π_{DT} is from ref.[52]. This quantity is then used to compute the spectral slope to be compared with the S_{VIS} temporal profiles measured by VIRTIS-M for the Imhotep ROI. The best fit of the spectral slope at each given time provides the corresponding areal fraction of BP in the investigated ROI (f_b).

For the Hapi region we also modelled the effects of a minor enrichment of water in the dark terrain. This is obtained by modifying the single scattering albedo of the dark terrain w_{DT} in Eq. 20 into w^*_{DT}, where

$$w^*_{DT} = f^*_I w_I + (1 - f^*_I) w_{DT} \tag{25}$$

with f^*_I representing the ice fraction.

Semi-transparent dehydrated crust scenario

One of the outputs of the water-driven activity model by ref.[10] is the smallest size s_m of the ejected dust, ranging from about 1 mm at a heliocentric distance of 3.5 au, down to 10 μm at 67P's perihelion (1.23 au). Assuming the surface would develop a dehydrated crust as the effect of water-ice-sublimation, s_m would represent its thickness, being the maximum depth at which sublimation may occur without removing dust. Let's assume that this crust is transparent to VIRTIS, which then can receive light scattered by the ice-rich layers below the crust, upon attenuation by the crust's optical thickness. In particular, for decreasing crust optical depths, the signal coming from the subsurface ice undergoes a smaller attenuation and the resulting spectral slope of the surface would become progressively bluer. If most of the nucleus has about the same ice content below the crust, for a given crust thickness, the colour observed by VIRTIS is a proxy of the nucleus ice content.

The thickness s_m depends directly on the surface temperature[10]: the higher the temperature, the smaller s_m. It follows that, for a given amount of subsurface ice, the colour measured by VIRTIS should provide a direct measurement of the crust thickness and by consequence of the surface temperature. Independent measurements of colour (VIRTIS-M VIS channel) and temperature (from thermal emission by means of the VIRTIS-M IR channel[20]) evidence that this is not the case: VIRTIS in fact measures different temperatures in areas having the same colour, and different colours in areas having the same temperature. In particular, this is found when the average spectral slope in Hapi and Imhotep are compared. In August 2014, when the comet was at approximately 3.5 au, Hapi was characterised by an average spectral slope of (17.7±0.7) %/(100 nm), as derived by averaging VIRTIS-M observations falling in an area comprised

in the latitude 60°-75° and longitude 270°-315° intervals, and the surface temperature is of the order of 220 K (ref.[20]). Such value of the spectral slope is comparable with the colour observed in Imhotep in June 2015 (≈ 1.45 au, after VIRTIS-M-IR cryocooler failure in May 2015), when the surface temperature would be significantly higher: this can be inferred from the measured[20] $T = 232$ K in Imhotep already in April 2015 (≈ 1.9 au). Moreover in April 2015, Imhotep's spectral slope is $S_{VIS} = (19.9 \pm 0.7)$ %/(100 nm), a value larger than Hapi's, which is characterised by a lower temperature. The above discussions indicates that the surface colour variability observed by VIRTIS cannot be explained in terms of crust thickness variability over an ice-rich layer.

Moreover crusts thinner than the pebble size $2R$ are also inconsistent with the model[10] itself. Such a size $2R$ can be interpreted as the size of the dust agglomerates which have been assumed isothermal[10], so that the gas pressure due to diffusion inside the agglomerates overcomes the tensile strength bonding the dust particles to the pebble. The pebble radius R drives the water loss flux Q_g from the nucleus[10]: the larger the radius R, the smaller the flux Q_g, and the larger the nucleus area A required to fit the observed water loss rate $Q_w = AQ_g$. In August 2014 we have $Q_w = 1.2$ kg/s (ref.[54]), which, with a pebble radius $R = 5$ mm and the corresponding water loss flux $Q = 2.3 \times 10^{-7}$ kg m^{-2} s^{-1}, yields $A = 5$ km^2. Measurements of Hapi's erosion have shown that on August 2014 the entire Hapi region was uniformly eroded[41]. Since Hapi has $A \approx 2$ km^2 (ref.[39]), we obtain that the size of the isothermal units where gas diffusion occurs is at least 4 mm (all the water flux coming from Hapi). Assuming that all northern fallout deposits of total $A = 10$ km^2 (ref.[39]) behave as Hapi[42], we get the upper limit of the size of the isothermal units of 20 mm. Since the best estimates of the radius of the pebbles is $R = 5$ mm (ref.[12]), we can conclude that the sunlit pebbles are almost perfectly isothermal. Given that the dehydration of isothermal pebbles is necessarily uniform in all their volume, the crust of cometary nuclei must be at least one pebble thick. This also makes it impossible to explain surface colour variability in terms of crust thickness, as a crust thicker than $2R$ =1 cm would be completely opaque to observations at visible wavelengths.

The colour of Hapi

According to our result, the activity over large part of the comet surface can be explained by discrete sources (BPs) scattered in a larger dehydrating surface. The same description, however, cannot be applied to the Hapi region, which in fact was uniformly active in August 2014[41]. With a surface temperature as high as T= 220 K (ref.[20]), activity in Hapi is possible if the whole surface is characterised by $\delta < 10^3$ (ref.[10]). As mentioned above, in August 2014 (3.5 au), a reference value for the Hapi spectral slope is $S_{VIS} = (17.7 \pm 0.7)$ %/(100 nm). The observed colour is matched either modelling Hapi's surface as a homogeneous intimate mixture of the comet dark terrain and 1-1.5% water ice ($\delta \approx$ 131-200), or assuming an areal mixture of water-ice-enriched dark terrain (intimate mixture with 0.2 % volume of ice, corresponding to $\delta \approx 10^3$) and 1.1-1.9% of BPs. Both these paradigms are compatible with Hapi being uniformly active in August 2014, and require roughly a total ice volumetric abundance of 1% (≈ 0.5% in mass), in agreement with independent estimations[41] obtained by measurements of Hapi's erosion rate, which provide an ice mass fraction of 1.2 ± 0.8%. Hapi and the other northern deposits on 67P, are probably covered by fallout, emitted by the active southern territories close to perihelion[43]. This process is supported by our estimation of the average water-ice abundance in Hapi (≈ 1%) as obtained from VIRTIS-M observations, being fairly close to the amount of water ice inferred on Imhotep at perihelion. Compatibly with the result of our simulations, which provides a larger fraction of BPs exposed on the surface for increasing CO_2 erosion, the volumetric ice fraction in Imhotep, in fact, can be considered a lower limit of the abundance of exposed ice in the southern hemisphere at perihelion, given the more intense insolation conditions in the latter case[28] consistent with an additional loss of water ice after ejection[34]. As all Hapi is expected to be characterised by $\delta < 10^3$, water ice has to be intimately mixed

with the refractory materials at sub-pebble scale across the whole surface. This requires redistribution and mixing of the water ice coming from the southern BPs. In this respect, we may expect that, as a consequence of the fallout, the ice-rich chunks originating from the southern BPs would be evenly distributed across Hapi at spatial scales of several-chunks-size. In addition, further homogenisation of the water ice distribution at sub-pebble scale can be provided by the diurnal cycle of sublimation and re-condensation observed in Hapi, which acts on the scale length of the diurnal thermal skin depth, of the order of few centimetres[19].

Southern hemisphere erosion and expected blueing at perihelion

In the period from 2015 July 24 to 2015 September 15 the active part of the southern hemisphere of comet 67P underwent an average erosion by chunks ejection of ≈ 4-10 m (refs.[10,34]). Assuming such value of erosion we can estimate the expected BP-fraction on the southern hemisphere surface by means of our modelling (see Methods). For simplicity, we assume constant insolation conditions in the southern hemisphere for this period, being in polar summer[28], with a water-driven erosion $E = 13$ cm/day^{-1} (ref.[10]). In stationary conditions, the increase of BP in the time interval $[t, t+dt]$ can be expressed as

$$\frac{dBP_{South}}{dt} = f_{CO_2}(f_{WEB} - BP_{South}) - \frac{BP_{South}}{\Delta t}, \tag{26}$$

where BP_{South} is the surface fraction of the active southern hemisphere covered in BPs in the stationary regime, Δt is the time of erosion of a BP due to the combined effect of H_2O, and CO_2 erosion and the term $BP_{South}/\Delta t$ is the areal fraction of BP removed per unit time. The latter stems from the fact that all the BPs on the surface at a given time $t - \Delta t$ are completely eroded by the time t, thus the BP removal rate is $BP_{South}/\Delta t$. Assuming a constant CO_2 areal fraction erosion rate $f_{CO_2} = K$, we have that the average vertical CO_2 erosion rate is given by $K * L_c$, where L_c is the emitted chunk size. K is defined from the total erosion E_{tot} in chunks of size L_c in the 53-days-period P from 2015 July 24 to 2015 September 15, which is expressed by $E_{tot} = K * P * L_c$, and gives $K = \frac{E_{tot}}{P * L_c}$. Finally, Δt depends on the WEB size L and the H_2O and CO_2 erosion rates as $\Delta t = \frac{L}{K * L_c + E}$. In the stationary regime we have $dBP_{South}/dt = 0$ and Eq. 26 can be solved straightforwardly providing

$$BP_{South} = \frac{K}{1/\Delta t + K} f_{WEB}. \tag{27}$$

In Methods, we defined combinations of L and f_{WEB} which provide a BP temporal evolution compatible with the one observed in Imhotep. Our results indicate that WEB sizes smaller than ≈ 1 m are required, with f_{WEB} decreasing with increasing L. Assuming the same WEB physical properties across the whole nucleus, we can use the values of L and f_{WEB} inferred from the Imhotep ROI analysis to compute the expected surface fraction of BP in the active southern hemisphere from Eq. 27. We investigated four possible combinations accounting for the two extreme erosion cases, $E_{tot} = 4$ m (ref.[34]) and $E_{tot} = 10$ m (ref.[10]), and two slightly different values of the chunk size, $L_c = 0.1$ m (as for the Imhotep ROI models) and $L_c = 0.13$ m (more representative of the southern hemisphere at perihelion[34]). In Fig. S5, BP_{South} is reported against L and is compared with the upper limit of the water-driven eroded areas ($\delta < 5$). This upper limit is originally estimated to ≈ 4% (ref.[10]), but we adopt a more conservative value of 6%, including uncertainties affecting the dust and water loss rates[10]. BP_{South} decreases with increasing L. These results indicate that only $L \gtrsim 0.5$ m provides values of BP_{South} compatible with the upper limit on water-active areas. As a matter of fact, this constrains the WEB size to $\approx 0.5 - 1$ m, as WEBs larger than 1 m are not compatible with the upper limit on the WEB size, from the Imhotep ROI analysis. For L ≈0.5-1 m we obtain $BP_{South} \approx 6 - 4\%$, which is relatively close to the value measured in the Imhotep ROI in the same

period (≈ 2%), and in qualitative agreement with the observed southern hemisphere colour at perihelion being similar to the rest of the nucleus[8]. If only half of the southern hemisphere is active at perihelion[10], and active and non-active areas are mixed at a few-metre scale, the final amount of BPs would be half of BP_{South}, thus even closer to the values in Imhotep. However, there are no clear observation evidences in this respect. WEBs much smaller than 0.5 m, along with exceeding the upper limit of water-driven eroded areas, would result in a southern hemisphere colour at perihelion much bluer than the rest of the surface. The possibility to describe with a single set of WEB properties the occurrence of BPs (i.e. water-driven eroded areas) across different regions of the comet (Imhotep and the southern hemisphere), supports the scenario of a uniform distribution of WEBs in the 67P nucleus, as per our proposed cometary nucleus model.

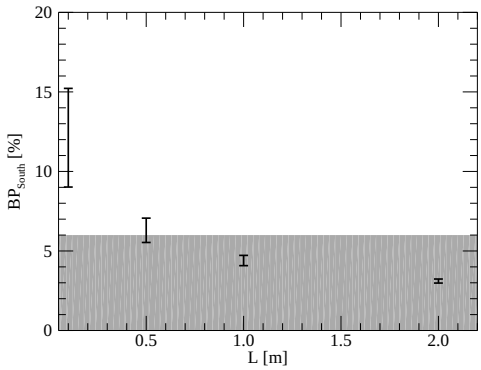

Figure S5. BP_{South} as a function of the WEB size L. For each point the bars span from a minimum to a maximum value, corresponding to the extreme BP_{South} values obtained by combining E_{tot} =4 m, 10 m, and L_c = 0.1 m, 0.13 m. The grey band represents BP_{South} values compatible with the 6% upper limit of water-active areas in the active southern hemisphere.

Post-perihelion fallout effects

The BP temporal evolution models of Fig. 4 with WEB size $L = 0.5 - 1$ m provide a good match to the observed behaviour up to December 2015. Later, the predicted evolution overestimates the amount of BPs observed on the surface. We interpret the steeper-than-simulations BP fraction decrease after perihelion as the effect of the fallout of material ejected at perihelion from the southern hemisphere and then covering the BPs. Such process is not explicitly included in our surface evolution model, whereas its post-perihelic effect was anticipated by requiring our simulations to match the BP temporal evolution only up to September 2015 (maximum blueing). As shown above, the fallout material has an average water-ice content of a few percent when ejected by the southern hemisphere. If the fallout material gets dehydrated to an average dust-to-water-ice mass ratio $\delta > 10^3$ after ejection, once deposited on the surface (in particular on the BPs), it results in nucleus spectral reddening and in a reduction of the effective estimated BP fraction. Ref.[34] estimates the fallout at 80% of the ejected mass. Southern erosions from 4 m (ref.[34], eroded surface of 20% of the total one) to 10 m (ref.[10], eroded surface of 10% of the total one) imply an average fallout on the nucleus 0.6–0.8 m thick. Starting from mid-May 2016 and up to early August 2016, the insolation conditions in Imhotep are such that accumulated fallout material with $10^3 < \delta < 10^4$ (Fig. 6) would undergo water-driven erosion. This would allow fallout self-cleaning, and, with the erosion rate reported in Fig. 7, we estimate a total erosion of ≈ 0.5 m from mid-May 2016 to early August 2016, when water-driven erosion stops. This value differs from the average amount of fallout

blanketing 67P surface less than the depth of the CO_2 sublimation front, indicating that the Imhotep region self-cleans from fallout by August 2016, thus exposing a pristine surface at the next inbound phase. This also indicates that the net erosion in the Imhotep region during one orbit[41] is mostly CO_2-driven, and that CO_2-driven erosion effectively can expose WEBs starting from roughly February 2015, ensuring the replicability of the seasonal colour cycle at each orbit.

The ongoing self-cleaning in Hapi (upper left panel in Fig. 2) exposes a much bluer interior of the chunks composing the fallout than the ongoing self-cleaning in Imhotep (upper right panel in Fig. 2), i.e. the fallout in Imhotep has an average δ significantly larger than in Hapi. Since Hapi is a nucleus concavity, opposite to convex Imhotep, the different fallout's δ may be related to the dominant fast (ballistic) fallout into Hapi with respect to a much slower (spiraling down from bound orbits[44]) fallout into Imhotep, in fact lasting many months (Fig. 4). The fast ballistic fallout into Hapi occurs during Hapi's polar night, and exposes water ice in the chunk crust by thermal inversion[19]. In the orbiting chunks of the slow spiraling fallout, this process occurs at every eclipse to sunlight by the nucleus, triggering the erosion of the chunks (with δ low enough) as they exit out of the eclipse back to sunlight. This process selects a slow spiraling fallout much drier than the fast ballistic one.

Data availability

The VIRTIS calibrated data are publicly available through the European Space Agency's Planetary Science Archive website (https://archives.esac.esa.int/psa/).

References

1. Sunshine, J. M. *et al.* Exposed Water Ice Deposits on the Surface of Comet 9P/Tempel 1. *Science* **311**, 1453–1455, DOI: 10.1126/science.1123632 (2006).

2. Filacchione, G. *et al.* Exposed water ice on the nucleus of comet 67P/Churyumov-Gerasimenko. *Nature* **529**, 368–372, DOI: 10.1038/nature16190 (2016).

3. Raponi, A. *et al.* The temporal evolution of exposed water ice-rich areas on the surface of 67P/Churyumov-Gerasimenko: spectral analysis. *Mon. Notices Royal Astron. Soc.* **462**, S476–S490, DOI: 10.1093/mnras/stw3281 (2016). 1612.02231.

4. Barucci, M. A. *et al.* Detection of exposed H_2O ice on the nucleus of comet 67P/Churyumov-Gerasimenko. as observed by Rosetta OSIRIS and VIRTIS instruments. *Astron. Astrophys.* **595**, A102, DOI: 10.1051/0004-6361/201628764 (2016).

5. Oklay, N. *et al.* Long-term survival of surface water ice on comet 67P. *Mon. Notices Royal Astron. Soc.* **469**, S582–S597, DOI: 10.1093/mnras/stx2298 (2017).

6. Taylor, M. G. G. T., Altobelli, N., Buratti, B. J. & Choukroun, M. The Rosetta mission orbiter science overview: the comet phase. *Philos. Transactions Royal Soc. Lond. Ser. A* **375**, 20160262, DOI: 10.1098/rsta.2016.0262 (2017). 1703.10462.

7. Ciarniello, M. *et al.* The global surface composition of 67P/Churyumov-Gerasimenko nucleus by Rosetta/VIRTIS. II) Diurnal and seasonal variability. *Mon. Notices Royal Astron. Soc.* **462**, S443–S458, DOI: 10.1093/mnras/stw3177 (2016).

8. Fornasier, S. *et al.* Rosetta's comet 67P/Churyumov-Gerasimenko sheds its dusty mantle to reveal its icy nature. *Science* **354**, 1566–1570, DOI: 10.1126/science.aag2671 (2016).

9. Filacchione, G. *et al.* An orbital water-ice cycle on comet 67P from colour changes. *Nature* **578**, 49–52, DOI: 10.1038/s41586-020-1960-2 (2020).

10. Fulle, M. *et al.* How comets work: nucleus erosion versus dehydration. *Mon. Notices Royal Astron. Soc.* **493**, 4039–4044, DOI: 10.1093/mnras/staa508 (2020).

11. Gundlach, B., Fulle, M. & Blum, J. On the activity of comets: understanding the gas and dust emission from comet 67/Churyumov-Gerasimenko's south-pole region during perihelion. *Mon. Notices Royal Astron. Soc.* **493**, 3690–3715, DOI: 10.1093/mnras/staa449 (2020).

12. Blum, J. *et al.* Evidence for the formation of comet 67P/Churyumov-Gerasimenko through gravitational collapse of a bound clump of pebbles. *Mon. Notices Royal Astron. Soc.* **469**, S755–S773, DOI: 10.1093/mnras/stx2741 (2017). 1710.07846.

13. Filacchione, G. *et al.* Seasonal exposure of carbon dioxide ice on the nucleus of comet 67P/Churyumov-Gerasimenko. *Science* **354**, 1563–1566, DOI: 10.1126/science.aag3161 (2016).

14. Veverka, J. *et al.* Return to Comet Tempel 1: Overview of Stardust-NExT results. *Icarus* **222**, 424–435, DOI: 10.1016/j.icarus.2012.03.034 (2013).

15. Groussin, O. *et al.* Temporal morphological changes in the Imhotep region of comet 67P/Churyumov-Gerasimenko. *Astron. Astrophys.* **583**, A36, DOI: 10.1051/0004-6361/201527020 (2015). 1509.02794.

16. Pajola, M. *et al.* The pristine interior of comet 67P revealed by the combined Aswan outburst and cliff collapse. *Nat. Astron.* **1**, 0092, DOI: 10.1038/s41550-017-0092 (2017).

17. El-Maarry, M. R. *et al.* Surface changes on comet 67P/Churyumov-Gerasimenko suggest a more active past. *Science* **355**, 1392–1395, DOI: 10.1126/science.aak9384 (2017).

18. Fornasier, S. *et al.* Surface evolution of the Anhur region on comet 67P/Churyumov-Gerasimenko from high-resolution OSIRIS images. *Astron. Astrophys.* **630**, A13, DOI: 10.1051/0004-6361/201834824 (2019). 1903.09017.

19. De Sanctis, M. C. *et al.* The diurnal cycle of water ice on comet 67P/Churyumov-Gerasimenko. *Nature* **525**, 500–503, DOI: 10.1038/nature14869 (2015).

20. Tosi, F. *et al.* The changing temperature of the nucleus of comet 67P induced by morphological and seasonal effects. *Nat. Astron.* **3**, 649–658, DOI: 10.1038/s41550-019-0740-0 (2019).

21. Hansen, K. C. *et al.* Evolution of water production of 67P/Churyumov-Gerasimenko: An empirical model and a multi-instrument study. *Mon. Notices Royal Astron. Soc.* **462**, S491–S506, DOI: 10.1093/mnras/stw2413 (2016).

22. Filacchione, G. *et al.* The global surface composition of 67P/CG nucleus by Rosetta/VIRTIS. (I) Prelanding mission phase. *Icarus* **274**, 334–349, DOI: 10.1016/j.icarus.2016.02.055 (2016). 1602.09098.

23. Longobardo, A. *et al.* 67P/Churyumov-Gerasimenko active areas before perihelion identified by GIADA and VIRTIS data fusion. *Mon. Notices Royal Astron. Soc.* **483**, 2165–2176, DOI: 10.1093/mnras/sty3244 (2019).

24. Coradini, A. *et al.* Virtis: An Imaging Spectrometer for the Rosetta Mission. *Space Sci. Rev.* **128**, 529–559, DOI: 10.1007/s11214-006-9127-5 (2007).

25. Capaccioni, F. *et al.* The organic-rich surface of comet 67P/Churyumov-Gerasimenko as seen by VIRTIS/Rosetta. *Science* **347**, 628, DOI: 10.1126/science.aaa0628 (2015).

26. Fornasier, S. *et al.* Spectrophotometric properties of the nucleus of comet 67P/Churyumov-Gerasimenko from the OSIRIS instrument onboard the ROSETTA spacecraft. *Astron. Astrophys.* **583**, A30, DOI: 10.1051/0004-6361/201525901 (2015). 1505.06888.

27. El-Maarry, M. R. *et al.* Regional surface morphology of comet 67P/Churyumov-Gerasimenko from Rosetta/OSIRIS images: The southern hemisphere. *Astron. Astrophys.* **593**, A110, DOI: 10.1051/0004-6361/201628634 (2016).

28. Keller, H. U. *et al.* Insolation, erosion, and morphology of comet 67P/Churyumov-Gerasimenko. *Astron. Astrophys.* **583**, A34, DOI: 10.1051/0004-6361/201525964 (2015).

29. Jorda, L. *et al.* The global shape, density and rotation of Comet 67P/Churyumov-Gerasimenko from preperihelion Rosetta/OSIRIS observations. *Icarus* **277**, 257–278, DOI: 10.1016/j.icarus.2016.05.002 (2016).

30. Keller, H. U. *et al.* OSIRIS The Scientific Camera System Onboard Rosetta. *Space Sci. Rev.* **128**, 433–506, DOI: 10.1007/s11214-006-9128-4 (2007).

31. Fulle, M. *et al.* Comet 67P/Churyumov-Gerasimenko preserved the pebbles that formed planetesimals. *Mon. Notices Royal Astron. Soc.* **462**, S132–S137, DOI: 10.1093/mnras/stw2299 (2016).

32. Colangeli, L. *et al.* The Grain Impact Analyser and Dust Accumulator (GIADA) Experiment for the Rosetta Mission: Design, Performances and First Results. *Space Sci. Rev.* **128**, 803–821, DOI: 10.1007/s11214-006-9038-5 (2007).

33. Ott, T. *et al.* Dust mass distribution around comet 67P/Churyumov-Gerasimenko determined via parallax measurements using Rosetta's OSIRIS cameras. *Mon. Notices Royal Astron. Soc.* **469**, S276–S284, DOI: 10.1093/mnras/stx1419 (2017).

34. Fulle, M. *et al.* The refractory-to-ice mass ratio in comets. *Mon. Notices Royal Astron. Soc.* **482**, 3326–3340, DOI: 10.1093/mnras/sty2926 (2019).

35. De Sanctis, M. C. *et al.* Shape and obliquity effects on the thermal evolution of the Rosetta target 67P/Churyumov-Gerasimenko cometary nucleus. *Icarus* **207**, 341–358, DOI: 10.1016/j.icarus.2009.11.009 (2010).

36. Capria, M. T. *et al.* How pristine is the interior of the comet 67P/Churyumov–Gerasimenko? *Mon. Notices Royal Astron. Soc.* **469**, S685–S694, DOI: 10.1093/mnras/stx2627 (2017). https://academic.oup.com/mnras/article-pdf/469/Suppl_2/S685/22064544/stx2627.pdf.

37. O'Rourke, L. *et al.* The philae lander reveals low-strength primitive ice inside cometary boulders. *Nature* **586**, 697–701, DOI: 10.1038/s41586-020-2834-3 (2020).

38. Zakharov, V. V., Crifo, J. F., Rodionov, A. V., Rubin, M. & Altwegg, K. The near-nucleus gas coma of comet 67P/Churyumov-Gerasimenko prior to the descent of the surface lander PHILAE. *Astron. Astrophys.* **618**, A71, DOI: 10.1051/0004-6361/201832883 (2018).

39. Thomas, N. *et al.* Regional unit definition for the nucleus of comet 67P/Churyumov-Gerasimenko on the SHAP7 model. *Planet. Space Sci.* **164**, 19–36, DOI: 10.1016/j.pss.2018.05.019 (2018).

40. Hu, X. *et al.* Seasonal erosion and restoration of the dust cover on comet 67P/Churyumov-Gerasimenko as observed by OSIRIS onboard Rosetta. *Astron. Astrophys.* **604**, A114, DOI: 10.1051/0004-6361/201629910 (2017).

41. Cambianica, P. *et al.* Time evolution of dust deposits in the Hapi region of comet 67P/Churyumov-Gerasimenko. *Astron. Astrophys.* **636**, A91, DOI: 10.1051/0004-6361/202037485 (2020).

42. Cambianica, P. *et al.* Long-term measurements of the erosion and accretion of dust deposits on comet 67P/Churyumov-Gerasimenko with the OSIRIS instrument. *Mon. Notices Royal Astron. Soc.* DOI: 10.1093/mnras/stab950 (2021). Stab950, https://academic.oup.com/mnras/advance-article-pdf/doi/10.1093/mnras/stab950/37008172/stab950.pdf.

43. Keller, H. U. *et al.* Seasonal mass transfer on the nucleus of comet 67P/Chuyumov-Gerasimenko. *Mon. Notices Royal Astron. Soc.* **469**, S357–S371, DOI: 10.1093/mnras/stx1726 (2017). 1707.06812.

44. Bertini, I. *et al.* The backscattering ratio of comet 67P/Churyumov-Gerasimenko dust coma as seen by OSIRIS onboard Rosetta. *Mon. Notices Royal Astron. Soc.* **482**, 2924–2933, DOI: 10.1093/mnras/sty2843 (2019).

45. Ciarletti, V. *et al.* CONSERT constrains the internal structure of 67P at a few metres size scale. *Mon. Notices Royal Astron. Soc.* **469**, S805–S817, DOI: 10.1093/mnras/stx3132 (2017).

46. Terada, H. *et al.* Detection of water ice in edge-on protoplanetary disks: HK tauri b and HV tauri c. *The Astrophys. J.* **667**, 303–307, DOI: 10.1086/520951 (2007).

47. Min, M. *et al.* The abundance and thermal history of water ice in the disk surrounding hd527 from the digit herschel key program. *Astron. Astrophys.* **593**, A11, DOI: 10.1051/0004-6361/201425432 (2016).

48. Pätzold, M. *et al.* The Nucleus of comet 67P/Churyumov-Gerasimenko - Part I: The global view - nucleus mass, mass-loss, porosity, and implications. *Mon. Notices Royal Astron. Soc.* **483**, 2337–2346, DOI: 10.1093/mnras/sty3171 (2019).

49. Acton, C. H. Ancillary data services of NASA's Navigation and Ancillary Information Facility. *Planet. Space Sci.* **44**, 65–70, DOI: 10.1016/0032-0633(95)00107-7 (1996).

50. Bertini, I. *et al.* Search for satellites near comet 67P/Churyumov-Gerasimenko using Rosetta/OSIRIS images. *Astron. Astrophys.* **583**, A19, DOI: 10.1051/0004-6361/201525979 (2015).

51. Magrin, S. *et al.* Pre-hibernation performances of the osiris cameras onboard the rosetta spacecraft. *Astron. Astrophys.* **574**, A123, DOI: 10.1051/0004-6361/201423830 (2015).

52. Ciarniello, M. *et al.* Photometric properties of comet 67P/Churyumov-Gerasimenko from VIRTIS-M onboard Rosetta. *Astron. Astrophys.* **583** (2015).

53. Hapke, B. *Theory of reflectance and emittance spectroscopy* (Cambridge University Press, 2012).

54. Gulkis, S. *et al.* Subsurface properties and early activity of comet 67P/Churyumov-Gerasimenko. *Science* **347**, aaa0709, DOI: 10.1126/science.aaa0709 (2015).